31st Congress of the International Council of the Aeronautical Sciences

Belo Horizonte, Brazil; September 09-14, 2018

IONIZATION AND DISSOCIATION EFFECTS ON HYPERSONIC BOUNDARY-LAYER STABILITY

Fernando Miró Miró[*0], Ethan S. Beyak[0], Daniel Mullen[**], Fabio Pinna[*] and Helen L. Reed[**]**

[*]**Von Kármán Institute for Fluid Dynamics**

[**]**Texas A&M University**

Keywords: *Boundary Layer, Stability, Hypersonics, Reentry*

Abstract

The prediction of the transition onset location in the high-temperature environments characteristic of atmospheric reentries requires physical models that correctly capture the underlying physical mechanisms. The current work presents state-of-the-art thermodynamic and transport models for high-temperature dissociating and ionizing flows, and investigates the case of a 10-deg wedge during a Martian return mission. The early stages of transition are studied by means of linear stability theory and the basic-state flow fields are obtained combining inviscid and boundary layer theory.

1 Background

Accurately predicting the location of boundary-layer transition onset and breakdown is necessary for an optimized and reliable design of atmospheric entry and hypersonic vehicles. The drastic increase in surface heating associated with the change from the laminar to the turbulent regime of the boundary layer (up to a factor of 8 or more [1]) is a potential *mission killer*, and therefore plays a major role in the sizing of Thermal Protection Systems (TPS).

The early stages of transition in a low disturbance environment [2], where instabilities grow linearly and without interacting can be studied with Linear Stability Theory (LST) [3, 4]. More physically inclusive theories, such as the Linear Parabolized Stability Equations (LPSE) [5], Nonlinear Parabolized Stability Equations (NPSE) [6] or Direct Numerical Simulations (DNS) [7] allow to include successively larger ranges of the transitioning region.

Despite the efforts carried out throughout the last two decades, air dissociation and (specially) ionization still pose many fundamental questions about their effects on transition, even on the early stages of perturbation growth. Malik & Anderson [8] studied dissociation effects by investigating self-similar boundary layers in Local Thermodynamic Equilibrium (LTE) with LST. Stuckert & Reed [9] extended this analysis to boundary layers in chemical non-equilibrium. Hudson *et al.* [10] considered also thermal non-equilibrium effects by modeling the vibrational energy mode with a separate temperature from the translational and rotational. Mortensen & Zhong [11] included a surface chemistry model to account for the ablation of the TPS. Lyttle & Reed [12] and Franko *et al.* [13] carried out sensitivity studies to compare the effects of using different thermodynamic and transport models. Klentzman & Tumin [14] investigated viscosity effects on receptivity and stability in a dissociating binary oxygen mixture. Bitter & Shepherd [15] studied supersonic modes in vibrational non-equilibrium yet in chemically frozen, and Knisely & Zhong [16] extended their analysis to thermo-chemical non-equilibrium. Miró Miró *et al.* proposed an alternative compatibility boundary condition for the

[0]Correspondence authors:
fernando.miro.miro@vki.ac.be, ethanbeyak@gmail.com

species partial density perturbations [17], which significantly improved the conditioning of the matrix system, and then used it to study diffusion and strong chemistry effects on adiabatic-wall boundary layers [18]. More physically-inclusive techniques have also been employed in non-equilibrium flows, such as LPSE (see Malik [19] and Johnson [20]) or DNS (see Marxen *et al.* [21], Ma & Zhong [22] or Mortensen [11]).

The aforementioned work, investigated binary oxygen or five-species air mixtures, which only account for molecular dissociation. Convective and absolute instabilities in ionized mixtures have been investigated in plasma jet flows. Briggs [23] and Bers [24] analyze the underlying theoretical framework, which was then applied to gas jets by Michalke [25]. More recent work used LST [26] and Absolute Instability Theory [27] to analyze partially ionized plasma jet flows in the VKI-plasmatron facility assuming LTE conditions.

The study of the stability of partially ionized boundary layers in atmospheric reentry flows remains an untempered field of research. The present work addresses this void by looking at a 10-degree wedge in the peak heating of a Martian return mission [28, Ch. 1]. Different flow assumptions and air mixtures are compared, and their validity is assessed. The DEKAF basic-state solver [29] is extended with an inviscid Euler 1-D solver and with a marching boundary-layer solver, both accounting for dissociation and ionization. LST analyses are carried out using the VESTA toolkit [30], profiting of its automatic derivation and implementation capabilities [31].

2 Theoretical framework and methodology

The development of instabilities in the boundary layer around a wedge is studied by first resolving the laminar basic-state flow field, and then performing an LST analysis. The laminar basic state is obtained from solving the inviscid flow-field, and imposing the inviscid wall conditions on the boundary layer's free-stream boundary [32]. This assumption notedly neglects viscous-inviscid interaction normally occurring close to the leading edge. However, as pointed out by Brown [33], the corresponding transition predictions are valid as long as the interaction parameter is lower than one: $\mathrm{M}_\infty/\mathrm{Re}_{L,\infty}^{1/6} << 1$.

2.1 Flow assumptions and mixtures

Four different flow assumptions are compared. The most physically general is Chemical Non-Equilibrium (CNE), which allows for any chemical and flow time scales, and where air is considered as a dilute mixture of ideal gases. The thermodynamic and transport properties (dependent flow variables Q) are assumed to be functions of the flow temperature and species mass fractions $Q = Q(T, Y_s)$. $N_s - 1$ of these mass fractions require a specific concentration conservation equation. The N_s-th one can be obtained from enforcing the sum of the concentrations to be equal to one.

CNE is characterized by having non-zero species chemical source terms ($\dot{\omega}_s \neq 0$). Neglecting these source terms ($\dot{\omega}_s = 0$), and by extension the diffusion terms[1] ($J_s = 0$), one reaches a Thermally Perfect Gas (TPG) assumption. In TPG flows, Y_s is constant, which is why they are also referred to as frozen flows. This assumption is acceptable whenever the chemistry's characteristic time is significantly larger than that of the flow.

On the other hand, if the chemistry's characteristic time is overly faster than that of the flow, one can assume the flow to be in chemical equilibrium, hereafter referred to as LTE.[2] In LTE, neglecting elemental demixing,[3] the mole fractions are functions of temperature and pressure $X_s = X_s(p, T)$. This is to say, for each pressure and temperature there is a unique species composition corresponding to the equilibrium state (see

[1] In the absence of species source terms, there are no mole-fraction gradients ($\underline{\nabla} X_s = 0$) to drive the molecular diffusion.

[2] LTE (Local Thermodynamic Equilibrium) also assumes thermal equilibrium: all energy modes described with a single temperature. This is common to all studied flow assumptions.

[3] The elemental fractions $\mathcal{X}_E$ are considered to remain constant throughout the domain.

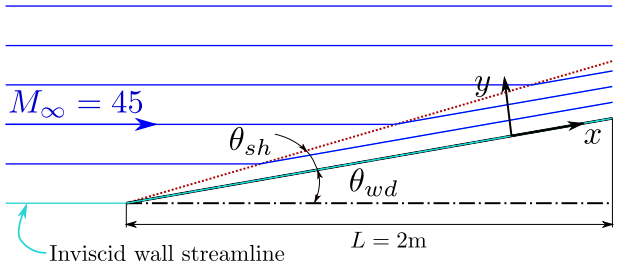

Fig. 1 : Sketch of the inviscid flowfield around the wedge.

appendix B). Since the system is in equilibrium, the chemical source terms are also zero ($\dot{\omega}_s = 0$).

The TPG assumption can be further simplified by considering the heat capacity to be constant ($c_p = \text{cst}$), reaching the Calorically Perfect Gas (CPG) assumption.

The commented functional dependency of the thermodynamic and transport properties remains unchanged for the aforementioned flow assumptions $Q = Q(T, Y_s)$. The difference between them is the origin of the mass fractions: obtained from solving separate concentration conservation equations in CNE, constant in TPG and CPG, and dependent on p and T through the equilibrium system in LTE. The only exceptions to this are the heat capacity and enthalpy in CPG: since c_p is enforced to be constant, h will be linear with temperature $h = c_p T$.

Three air mixtures are used:

- air-2: two-species air (N_2 and O_2) with constant mass fractions, used in CPG and TPG.
- air-5: five-species air (N, O, NO, N_2 and O_2), used in LTE and CNE.
- air-11: eleven-species air (e^-, N, N^+, O, O^+, NO, NO^+, N_2, N_2^+, O_2 and O_2^+), used in LTE and CNE.

The specific expressions for the thermodynamic and transport properties Q are detailed in appendix D. For an overview of the implications of the different flow assumptions, see Anderson [34, Ch. 10.4].

2.2 Inviscid flow

A sketch of the inviscid flowfield around the wedge is shown in Fig. 1. The shock jump relations for the different flow assumptions are detailed in appendix C. Neglecting the curving of the non-equilibrium shock, [4] all streamlines can be assumed parallel and the problem becomes one-dimensional. The inviscid wall conditions (coincident with the boundary layer edge) can therefore be obtained from solving the 1-D Euler equations along the wall streamline:

$$\frac{\mathrm{d}\rho_e u_e}{\mathrm{d}x} = 0\,, \tag{1a}$$

$$\rho_e u_e \frac{\mathrm{d}u_e}{\mathrm{d}x} + \frac{\mathrm{d}p_e}{\mathrm{d}x} = 0\,, \tag{1b}$$

$$\frac{\mathrm{d}h_e}{\mathrm{d}x} + u_e \frac{\mathrm{d}u_e}{\mathrm{d}x} = 0\,, \tag{1c}$$

$$\rho_e u_e \frac{\mathrm{d}Y_{s,e}}{\mathrm{d}x} = \dot{\omega}_{s,e}\,. \tag{1d}$$

In CPG, TPG and LTE, since the source term is zero $\dot{\omega}_{s,e} = 0$, the post-shock inviscid flowfield is constant in x. In CNE, Eqs. (1) are marched using the frozen post-shock conditions as an initial condition (see appendix C). For this purpose, an explicit 2^{nd}-order finite-difference marching solver is implemented into the DEKAF flow solver [29].

2.3 Boundary-layer flow

The inviscid wall profile is then imposed as a boundary condition to the steady boundary layer equations:

$$\frac{\partial \bar{\rho}\,\bar{u}}{\partial x} + \frac{\partial \bar{\rho}\,\bar{v}}{\partial y} = 0\,, \tag{2a}$$

$$\bar{\rho}\,\bar{u}\frac{\partial \bar{u}}{\partial x} + \bar{\rho}\,\bar{v}\frac{\partial \bar{u}}{\partial y} = -\frac{\mathrm{d}p_e}{\mathrm{d}x} + \frac{\partial}{\partial y}\left(\bar{\mu}\frac{\partial \bar{u}}{\partial y}\right)\,, \tag{2b}$$

$$\bar{\rho}\,\bar{u}\frac{\partial \bar{w}}{\partial x} + \bar{\rho}\,\bar{v}\frac{\partial \bar{w}}{\partial y} = \frac{\partial}{\partial y}\left(\bar{\mu}\frac{\partial \bar{w}}{\partial y}\right)\,, \tag{2c}$$

[4] This assumption is supported by the weak chemical activity observed in Fig. 3

$$\bar{\rho}\,\bar{u}\frac{\partial \bar{H}}{\partial x}+\bar{\rho}\,\bar{v}\frac{\partial \bar{H}}{\partial y}=\frac{\partial}{\partial y}\left(\bar{\kappa}\frac{\partial \bar{T}}{\partial y}\right)+\frac{\partial}{\partial y}\left(\bar{\mu}\,\bar{u}\frac{\partial \bar{u}}{\partial y}\right)+\bar{\mu}\left(\frac{\partial \bar{w}}{\partial y}\right)^2+\frac{\partial}{\partial y}\left(\sum_{s\in\mathcal{S}}\bar{h}_s\,\bar{\rho}_s\sum_{\ell\in\mathcal{S}}\bar{\mathcal{D}}_{s\ell}\frac{\partial \bar{X}_\ell}{\partial y}\right), \tag{2d}$$

$$\bar{\rho}\,\bar{u}\frac{\partial \bar{Y}_s}{\partial x}+\bar{\rho}\,\bar{v}\frac{\partial \bar{Y}_s}{\partial y}=\frac{\partial}{\partial y}\left(\bar{\rho}_s\sum_{\ell\in\mathcal{S}}\bar{\mathcal{D}}_{s\ell}\frac{\partial \bar{X}_\ell}{\partial y}\right)+\dot{\bar{\omega}}_s\,, \tag{2e}$$

$$\sum_{s\in\mathcal{S}}\bar{Y}_s=1\,, \tag{2f}$$

$$\sum_{s\in\mathcal{S}_{ion},e^-}\mathcal{Z}_s\,\bar{Y}_s=0\,, \tag{2g}$$

where Eq. (2f) enforces the sum of mass fractions to be equal to one, and Eq. (2g) enforces the ambipolar condition[5] (only necessary for ionized mixtures). The enforcement of these equations requires the matrix system to have only N_s-1 (non-ionized) or N_s-2 (ionized) species concentration conservation equations (2e).

The specific models used for the different thermodynamic, transport and chemical quantities (h, μ, κ, $\mathcal{D}_{s\ell}$, $\dot{\omega}_s$, etc.) can be found in appendix D.

Equations (2) are morphed using the Illingworth transformation and the non-dimensional quantities detailed in Ref. [29], leading to:

$$2\xi\,(\bar{f}_\eta\,\bar{f}_{\xi\eta}-\bar{f}_{\eta\eta}\,\bar{f}_\xi)=(\bar{C}\,\bar{f}_{\eta\eta})_\eta+\bar{f}\,\bar{f}_{\eta\eta}+\\+\beta_H\,(\bar{j}-\bar{f}_\eta^2)\,, \tag{3a}$$

$$2\xi\,(\bar{f}_\eta\,\bar{k}_\xi-\bar{k}_\eta\,\bar{f}_\xi)=(\bar{C}\,\bar{k}_\eta)_\eta+\bar{f}\,\bar{k}_\eta\,, \tag{3b}$$

$$2\xi\,(\bar{f}_\eta\,\bar{g}_\xi-\bar{g}_\eta\,\bar{f}_\xi)=(\bar{a}_1\,\bar{g}_\eta)_\eta+\bar{f}\,\bar{g}_\eta+\\-\theta_H\,\bar{f}_\eta\,\bar{g}+(\bar{a}_2\,\bar{f}_\eta\,\bar{f}_{\eta\eta})_\eta+\bar{a}_0\,\bar{k}_\eta^2+\\-\sum_{s\in\mathcal{S}}(\bar{a}_{1s}\,\bar{Y}_{s,\eta})_\eta+\sum_{s\in\mathcal{S}}\sum_{\ell\in\mathcal{S}}\left(\bar{a}_{2s\ell}\,(\bar{\zeta}_\ell\,\bar{Y}_\ell)_\eta\right)_\eta\,, \tag{3c}$$

$$2\xi\,(\bar{f}_\eta\,\bar{Y}_{s,\xi}-\bar{Y}_{s,\eta}\,\bar{f}_\xi)=\bar{f}\,\bar{Y}_{s,\eta}+\\+\sum_{\ell\in\mathcal{S}}\left(\bar{C}_{s\ell}\,(\bar{\zeta}_\ell\,\bar{Y}_\ell)_\eta\right)_\eta+2\xi\,\dot{\bar{\Omega}}_s\,, \tag{3d}$$

where the η and ξ subindices denote derivatives. The definition of the different non-dimensional variables and grouping parameters can be found in appendix A.

Note that for completeness Eqs. (2) and (3) are presented in their quasi-3D form[6] and without neglecting streamwise pressure or total enthalpy gradients[7]. However, for the analyzed wedge flow, these can be simplified enforcing $\beta_H=\theta_H=w_0=0$.

Equations (3) (together with (2f) and (2g)) are solved with DEKAF's boundary-layer solver [29], which has been extended to allow for streamwise marching. The self-similar system, obtained when dropping all ξ-marching terms (marked in blue), is solved with the methodology described in Ref [29]. For CPG, TPG and LTE, since $\dot{\bar{\Omega}}_s=0$ and the boundary-layer edge quantities are constant in ξ, the solution must not be marched.[8] The entire flowfield can therefore be retrieved by evaluating the self-similar solution at the different x locations. For the CNE assumption, the frozen (TPG) self-similar solution is marched in ξ retaining all terms in Eqs. (3).

The marching is done using a 2$^{\text{nd}}$-order finite-difference method on the computational equispaced grid $\chi\in[0,1]$. A mapping between χ and ξ allows to cluster points close to the leading edge, where there is a stronger chemical activity, yet maintaining a constant step at the downstream locations. This ensures also an appropriate point distribution for the relatively slower, yet non-zero, chemistry occurring in the boundary-layer edge. The mapping imposes a tanh-evolution of the streamwise step $\Delta\xi\propto\tanh(\chi)$, sketched in

[5] The net sum of the charges at all points of the domain must be zero.

[6] With a spanwise velocity w but with spanwise-invariant quantities $\partial/\partial z=0$.

[7] A non-zero total enthalpy gradient could come from a radiation source term for instance.

[8] These assumptions also do not require the resolution of the Y_s conservation equations (3d) or the concentration (2f) and ambipolar (2g) conditions.

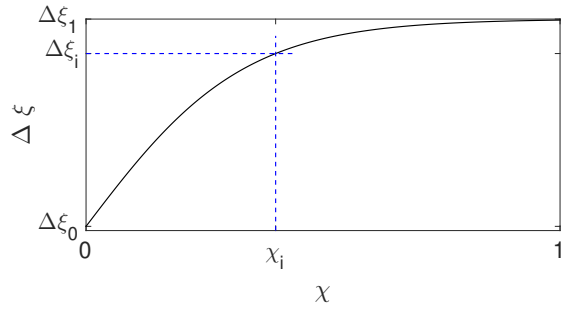

Fig. 2 : Sketch of the χ-ξ mapping's hyperbolic-tangent step.

Fig. 2, which leads to:

$$\xi(\chi) = \xi_0 + A_\chi \chi + B_\chi \ln(\cosh(a_\chi \chi)), \qquad (4)$$

where A_χ, B_χ and a_χ depend on the domain size, and the point clustering fixed through $\Delta\xi_0$, χ_i and the $\Delta\xi_i/\Delta\xi_1$ ratio:

$$A_\chi = \Delta\xi_0 (N_\chi - 1) \quad , \quad a_\chi = \frac{1}{\chi_i} \tanh^{-1}\left(\frac{\Delta\xi_i}{\Delta\xi_1}\right),$$
$$B_\chi = \frac{\xi_1 - \xi_0 - \Delta\xi_0 (N_\chi - 1)}{\ln(\cosh(a_\chi))}. \qquad (5)$$

2.4 Linear Stability Theory

The stability analyses performed on the laminar boundary-layer flowfields detailed in § 2.3, are carried out using LST. This theory decomposes the flow variables $q(x,y,z,t)$ into a basic-state $\bar{q}(y)$ and a perturbation component $q'(x,y,z,t)$. Subsequently substituting in the Navier-Stokes equations and linearizing, one obtains the perturbation equations. Finally a modal decomposition is performed by enforcing the LST ansatz:

$$q'(x,y,z,t) = \tilde{q}(y) \exp(-(\alpha x + \beta z - \omega t)) + \text{c.c.} \qquad (6)$$

where c.c. stands for complex conjugate.

The resulting stability equations form a generalized eigenvalue problem, which is solved to obtain the perturbation's complex α fixing real β and ω. The studied wedge configuration is well-known to be dominated by second-mode instabilities [3], which are 2-D waves with $\beta = 0$.

Stability analyses are carried out with the VESTA toolkit [30], with CPG, LTE, TPG and CNE solvers obtained with its Automatic Derivation and Implementation Tools [31]. The expressions for the CPG and LTE stability equations in cartesian coordinates implemented in VESTA may be found in Ref. [31]. The CNE and TPG Navier-Stokes equations in invariant form are detailed in Ref. [18], from which the stability equations are obtained by imposing the aforementioned assumptions.

Boundary conditions on the perturbation amplitude terms $\tilde{q}$ must be such that the homogeneity of the generalized eigenvalue problem is preserved. The wall boundary values are all fixed to zero, with the exception of the pressure $\tilde{p}$ (CPG and LTE solvers), the mixture density $\tilde{\rho}$ (TPG solver) or the species partial densities $\tilde{\rho}_s$ (CNE solver). Compatibility conditions for $\tilde{p}$ and $\tilde{\rho}$ are obtained from evaluating the y-momentum stability equation at the wall [3]. Similarly, the species y-momentum conservation equation is used to account for $\tilde{\rho}_s$ (see Ref. [17]). At the freestream, Neumann conditions are used for all perturbation amplitudes $\partial\tilde{q}/\partial y = 0$ [3].

An excellent overview of LST can be found in the works of Mack [3] and Arnal [4].

3 Results

The test conditions are chosen to coincide with the peak-heating point in a Martian return trajectory [28, Ch. 1], occurring at an altitude of approximately 45 km, and at a freestream Mach number of 45. At 45 km altitude, the International Standard Atmosphere's static pressure and temperature are $p_\infty = 146\,\text{Pa}$ and $T_\infty = 265\,\text{K}$. The freestream gas composition is fixed to $Y_{N_2,\infty} = 0.767$ and $Y_{O_2,\infty} = 0.233$. To avoid numerical overflow all other species mass fractions appearing in the different mixtures (see §2.1) are fixed to a very low non-zero trace value (10^{-10} for heavy particles and 10^{-30} for electrons). The sum of the traces is subtracted from a bath species (N_2) to ensure that the sum of the mass fractions equals one. The wall temperature is fixed to $T_w = 10000\,\text{K}$.

The considered geometry is a 10-degree 2-D wedge, of length $L = 2\,\text{m}$, as sketched in Fig. 1.

3.1 Basic state profiles

Figure 3 shows the evolution of the boundary-layer-edge properties as a function of x for each flow assumption. These are the wall conditions obtained from solving the appropriate shock jump relations (see appendix C), and the inviscid flowfield (see § 2.2). The inclination of the different shocks is summarized in table 1. As commented in § 2.2, for CPG, TPG and LTE, there is no variation of the flow quantities in the inviscid flow region, remaining constant and equal to the post-shock conditions.

The CPG shock jump is notedly stronger than the TPG shock, which is itself stronger than that of LTE. In CPG none of the freestream kinetic energy is assumed to be spent in exciting the internal energy modes, which have a higher thermal inertia, or in dissociating or ionizing. It is entirely directed to increasing temperature, through the translational mode, and pressure. The TPG shock is consequently weaker than that of CPG, yet due to it being assumed chemically frozen, it is stronger than that of LTE.

The only flow assumption modeling the streamwise evolution of the boundary-layer-edge properties is CNE. One may note that the pressure undershoots the LTE limit, caused by having neglected the CNE shock curving. This curving would bring the inviscid streamlines closer, slightly increasing the pressure and accelerating the flow. Nevertheless, this should not compromise the validity of the present analysis, since the difference in magnitude is minor, and pressure is in any case known to play a minor role on the chemical activity. The equilibrium composition, for instance, scales closer with the logarithm of pressure than with pressure itself.

Imposing these conditions at the edge boundaries, one can solve the flowfield in the boundary layer. Figure 4 shows the streamwise velocity, temperature and the N and N^+ mass fraction profiles, for the different flow assumptions.

Two CPG cases are compared, one with the commonly used transport models (Sutherland's law with a constant Prandtl number of 0.7), and another with the same model used for all other flow assumptions (Chapman-Enskog first approximation for viscosity and second for thermal conductivity). This allows to decouple the error introduced by the thermodynamic flow assumption and by the transport model. One can observe that Sutherland's law predicts stronger temperature gradients in the boundary layer, most likely due to the underestimation of the thermal conductivity (see Ref. [35]). However, it is worth noting that it appears to make a better estimation of the boundary-layer height, closer to the more accurate (TPG and CNE) models. This is believed to be a purely coincidental occurrence, in no way suggesting the model to be more accurate.

Flow assumption	Shock angle [deg]
CPG	12.17
TPG/CNE	11.71
LTE	11.38

Table 1: Shock angle with the different flow assumptions.

Successively incorporating the excitation of the internal energy modes (TPG), molecular dissociation in non-equilibrium (CNE with air-5) or in equilibrium (LTE with air-5), and ionization in non-equilibrium (CNE with air-11) or in equilibrium (LTE with air-11), contributes to reducing the temperature of the boundary layer. This is due to the increasing amount of energy directed to these phenomena.

Fig. 4 (c) demonstrates that ionization is clearly non-negligible under these conditions, since the N^+ ion reaches a maximum of 10% of the composition.

Comparing the results where non-equilibrium and equilibrium chemistry were assumed, one can see that the reduction of the flow speed close to the wall brings the non-equilibrium curves closer to equilibrium. In other words, there will be a strong change in the relative Damköhler number throughout the boundary layer.

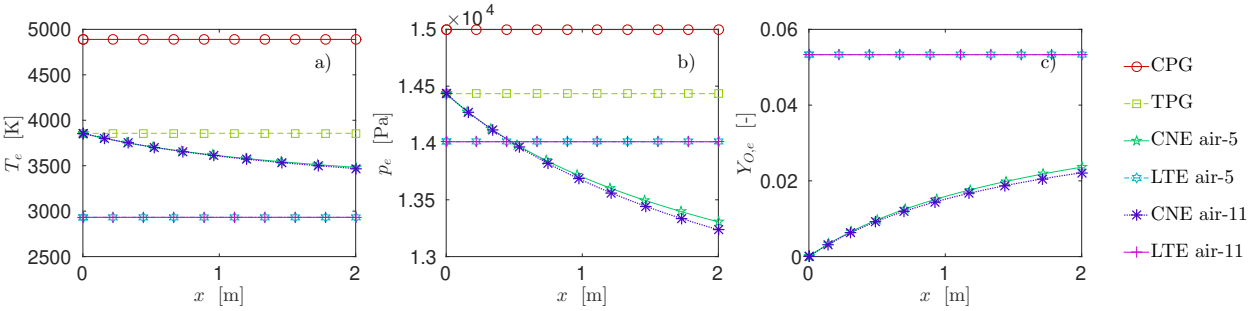

Fig. 3 : Streamwise evolution of the boundary-layer-edge conditions for each flow assumption.

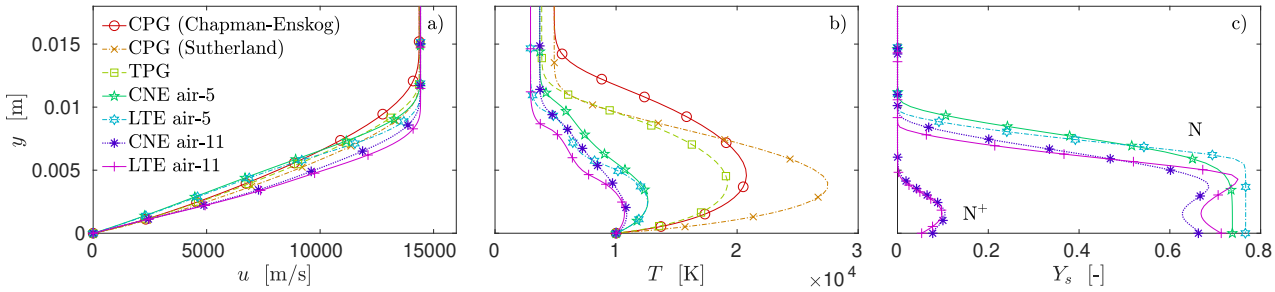

Fig. 4 : Laminar basic-state boundary-layer profiles at $x = 1\,\mathrm{m}$ for each flow assumption.

3.2 Perturbation growth rates at $x = 1\mathrm{m}$

LST analyses are then performed on the aforementioned flowfields, looking at the most unstable instability - Mack's second mode ($\beta = 0$). Figure 5 shows the comparison of the perturbation growth rates as a function of the perturbation frequency for the different flow assumptions, using the same transport model (Chapman-Enskog). One observes that the progressive inclusion of phenomena contributing to reducing the boundary-layer temperature (like the excitation of internal energy modes, molecular dissociation and ionization) destabilizes the second mode instabilities, and increases the range of unstable frequencies. This behavior may be explained by the enlargement of the region of relative supersonic flow close to the wall, and by the inviscid nature of the second mode, stabilized by the fluid's viscosity, which increases with temperature. The high-frequency content in the instantaneously reacting cases (LTE air-5 and air-11) in Fig. 5 suggests the appearance of supersonic modes. This is confirmed by looking at their eigenfunctions in Fig. 6, which display the characteristic radiation of energy into the freestream of such modes $|\tilde{T}|_{y>\delta_{99}}/|\tilde{T}|_{\max} \ll 1$.

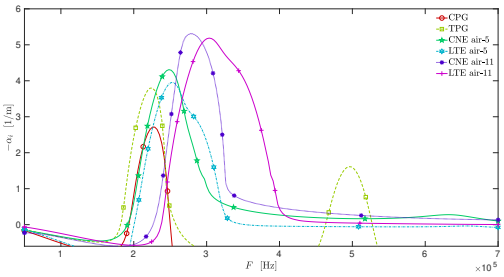

Fig. 5 : Perturbation growth rates as a function of the perturbation frequency at $x = 1\,\mathrm{m}$ for each flow assumption. All cases used the Chapman-Enskog transport models.

Figure 7 compares the two transport models used for the CPG flow assumption to the more accurate TPG and CNE air-11. One observes that Sutherland's law appears to give more accurate growth rate predictions, but as commented in § 3.1 this is simply coincidental. The results using the same transport model show the expected trend commented in the previous paragraph.

Finally, Fig. 8 analyzes the effect of using a

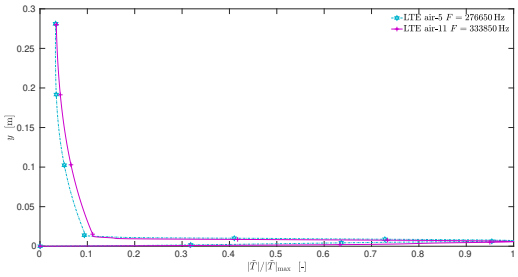

Fig. 6 : Supersonic modes with LTE flow assumptions at $x = 1$ m.

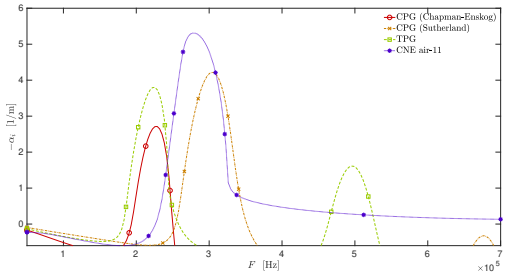

Fig. 7 : Effect on the perturbation growth rates of using different transport models in CPG.

different flow assumption on the basic-state and on the perturbation quantities. Three cases are compared:

- TPG basic state with TPG perturbations.
- CNE basic state with TPG perturbations (both for 5 and 11 species).
- CNE basic state with CNE perturbations (both for 5 and 11 species).

Similar previous analyses showed the results to be tremendously more sensitive to the basic-state assumption than the perturbation's [18]. However, Fig. 8 shows the CNE basic state with TPG perturbations cases to predict a much larger range of unstable frequencies than the CNE basic state with CNE perturbations cases. When integrating the perturbation amplification to obtain the e^N curves, this will presumably lead to a much sooner prediction of transition onset. It is also noteworthy that the third Mack mode appears to be strongly destabilized when assuming TPG perturbations, reaching practically the growth rate of the second mode.

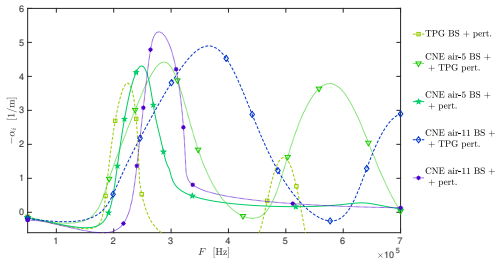

Fig. 8 : Perturbation growth rates as a function of the perturbation frequency at $x = 1$ m with different assumptions for the basic-state and perturbation quantities.

Figure 8 also shows the same behavior reported in Ref. [18]. The boundary-layer cooling introduced by the chemistry contributes to destabilize the flow, whereas the inclusion of the chemical activity in the perturbations has the opposite effect and actually stabilizes. There is therefore a trade-off, which in the observed ranges culminates in a destabilization of the boundary layer.

4 Conclusions

State-of-the-art thermodynamic and transport models were used to analyze the stability of a dissociating and ionizing boundary layer around a wedge in a Martian return mission.

The laminar basic-state flow field was obtained by firstly resolving the inviscid flow field, and then imposing the wall values at the edge of the boundary layer.

Several flow assumptions were compared, allowing an examination of the effect of successively incorporating more physical phenomena. The excitation of the internal energy modes, as well as molecular dissociation and ionization were all seen to contribute to reducing the overall temperature and size of the boundary layer. This reduction in temperature brought with it a larger region of relative supersonic flow close to the wall and a decrease in viscosity, which ultimately contributed to destabilizing the second mode.

The inclusion of ionization effects was seen

to significantly change the flow stability, suggesting that it is necessary to incorporate them in posterior analyses for similar flight conditions.

Supersonic modes, normally associated with highly cooled walls, were seen to appear for the highly reacting flow assumptions. This is despite having high wall temperatures ($T_w = 10000\,\mathrm{K}$), which suggests that the cooling of the boundary layer due to the chemical activity has the same effect as wall cooling.

The use of non-equilibrium perturbation models was also demonstrated to be necessary. Having a TPG perturbation assumption led to a substantial increase of the range of unstable frequencies, which will most likely result in larger integrated N factors, and premature transition onset predictions.

Acknowledgments

The authors would like to thank Koen Groot for his contribution to the implementation of DEKAF's marching algorithm.

This research was partially funded by the Belgian National Fund for Scientific Research (FNRS) through the FRIA fellowship.

Copyright Statement

The authors confirm that they, and/or their company or organization, hold copyright on all of the original material included in this paper. The authors also confirm that they have obtained permission, from the copyright holder of any third party material included in this paper, to publish it as part of their paper. The authors confirm that they give permission, or have obtained permission from the copyright holder of this paper, for the publication and distribution of this paper as part of the ICAS proceedings or as individual off-prints from the proceedings.

References

[1] E. R. V. Driest. Investigation of laminar boundary layer in compressible fluids using the crocco method. Technical Report TN 2597, NACA/North American Aviation Inc., Washington, January 1952.

[2] E. Reshotko. Paths to Transition in Wall Layers. In *Advances in laminar-turbulent transition modeling*, pages 1–8. von Karman Institute for Fluid Dynamics, 2008.

[3] L. M. Mack. Boundary-Layer Linear Stability Theory. In *Special Course on Stability and Transition of Laminar Flow, AGARD 709*. 1984.

[4] D. Arnal. Boundary layer transition: predictions based on linear theory. In *Special Course on Progress in Transition Modelling AGARD 793*. 1993.

[5] T. Herbert, G. Stuckert, and N. Lin. Method for Transition Prediction in High-Speed Boundary Layers. Technical report, WL-TR-93-3097. Air Force Materiel Command Wright-Patterson AFB, 1993.

[6] F. P. Bertolotti, T. Herbert, and P. R. Spalart. Linear and nonlinear stability of the Blasius boundary layer. *Journal of Fluid Mechanics*, 242:441–474, 1992.

[7] X. Zhong and X. Wang. Direct Numerical Simulation on the Receptivity, Instability, and Transition of Hypersonic Boundary Layers. *Annual Review of Fluid Mechanics*, 44(1):527–561, 2012.

[8] M. R. Malik and E. C. Anderson. Real gas effects on hypersonic boundarylayer stability. *Physics of Fluids*, 803(3):803–821, 1991.

[9] G. Stuckert and H. L. Reed. Linear Disturbances in Hypersonic, Chemically Reacting Shock Layers. *AIAA Journal*, 32(7):1384–1393, 1994.

[10] M. L. Hudson, N. Chokani, and G. V. Candler. Linear Stability of Hypersonic Flow in Thermochemical Non-equilibrium. *AIAA Journal*, 35(6):958–964, 1997.

[11] C. Mortensen and X. Zhong. Real-Gas and Surface-Ablation Effects on Hypersonic Boundary-Layer Instability over a Blunt Cone. *AIAA Journal*, 54(3):980–998, 2016.

[12] I. Lyttle and H. L. Reed. Sensitivity of Second-Mode Linear Stability to Constitutive Models within Hypersonic Flow. *AIAA paper*, 2005-889, 2005.

[13] K. J. Franko, R. W. MacCormack, and S. K. Lele. Effects of chemistry modeling on hypersonic boundary layer linear stability prediction. *AIAA paper*, 2010-4601, 2010.

[14] J. Klentzman and A. Tumin. Stability and receptivity of high speed boundary layers in oxygen. *AIAA paper*, 2013-2882, 2013.

[15] N. P. Bitter and J. E. Shepherd. Stability of highly cooled hypervelocity boundary layers. *Journal of Fluid Mechanics*, 778:586–620, 2015.

[16] C. P. Knisely and X. Zhong. Supersonic Modes in Hot-Wall Hypersonic Boundary Layers with Thermochemical Nonequilibrium Effects. *AIAA paper*, 2018-2085, 2018.

[17] F. Miró Miró and F. Pinna. Linear Stability Analysis of a Hypersonic Boundary Layer in Equilibrium and Non-Equilibrium. *AIAA paper*, 2017-4518, 2017.

[18] F. Miró Miró, F. Pinna, E. S. Beyak, P. Barbante, and H. L. Reed. Diffusion and chemical non-equilibrium effects on hypersonic boundary-layer stability. *AIAA paper*, 2018-1824, 2018.

[19] M. R. Malik. Hypersonic Flight Transition Data Analysis Using Parabolized Stability Equations with Chemistry Effects. *Journal of Spacecraft and Rockets*, 40(3):332–344, 2003.

[20] H. B. Johnson, J. E. Gronvall, and G. V. Candler. Reacting hypersonic boundary layer stability with blowing and suction. *AIAA paper*, 2009-938, 2009.

[21] O. Marxen, T. E. Magin, E. S. G. Shaqfeh, and G. Iaccarino. A method for the direct numerical simulation of hypersonic boundary-layer instability with finite-rate chemistry. *Journal of Computational Physics*, 255:572–589, 2013.

[22] Y. Ma and X. Zhong. Receptivity to Freestream Disturbances of a Mach 10 Nonequilibrium Reacting Oxygen Flow over A Flat Plate. *AIAA paper*, 2004-256, 2004.

[23] R. Briggs. *Electron-stream Interaction with Plasmas*. M.I.T. Press research monographs. M.I.T. Press, 1964.

[24] A. Bers. Space-time evolution of plasma instabilities - absolute and convective. In A. A. Galeev and R. N. Sudan, editors, *Handbook of Plasma Physics: Basic plasma physics I, Volume 1*, chapter 3.2. North Holland, 1983.

[25] A. Michalke. Survey on jet instability theory. *Progress in Aerospace Sciences*, 21:159–199, 1984.

[26] M. Chiatto. Numerical Study of Plasma Jets by Means of Linear Stability Theory. Technical Report VKI PR 2014-04, Von Kármán Institute for Fluid Dynamics, 2014.

[27] S. Demange, N. Kumar, M. Chiatto, and F. Pinna. Absolute instability in plasma jet. In *7th European Conference on Computational Fluid Dynamics*, Glasgow, UK, 2018.

[28] J. T. Howe. Hypervelocity Atmospheric Flight: Real Gas Flow Fields. Technical Report TM-101055, NASA, 1989.

[29] K. J. Groot, F. Miró Miró, E. S. Beyak, A. J. Moyes, F. Pinna, and H. L. Reed. DEKAF: spectral multi-regime basic-state solver for boundary layer stability. *AIAA paper*, 2018-3380, 2018.

[30] F. Pinna. VESTA toolkit: a Software to Compute Transition and Stability of Boundary Layers. *AIAA paper*, 2013-2616, 2013.

[31] F. Pinna and K. J. Groot. Automatic derivation of stability equations in arbitrary coordinates and different flow regimes. *AIAA paper*, 2014-2634, 2014.

[32] F. White. *Viscous Fluid Flow*. McGraw-Hill series in mechanical engineering. McGraw-Hill, 1991.

[33] S. N. Brown, A. F. Khorrami, A. Neish, and F. T. Smith. On hypersonic boundary-layer interactions and transition. *Philosophical Transactions of the Royal Society, Series A*, 335(1637):139–152, 1991.

[34] J. D. Anderson Jr. *Hypersonic and High Temperature Gas Dynamics*. American Institute of Aeronautics and Astronautics, Reston VA, second edition, 2006.

[35] J. B. Scoggins and T. E. Magin. Development of Mutation++: MUlticomponent Thermodynamics And Transport properties for IONized gases library in C++. *AIAA paper*, 2014-2966, 2014.

[36] L. Gurvich, I. Veyts, and C. Alcock. *Thermodynamic Properties of Individual Substances*. Hemisphere Publishing Corporation, 4 edition, 1989.

[37] J. B. Scoggins. *Development of numerical methods and study of coupled flow, radiation, and ablation phenomena for atmospheric entry*. PhD thesis, Université Paris-Saclay and VKI, 2017.

[38] S. Chapman and T. Cowling. *The Mathemati-*

cal Theory of Non-uniform Gases: An Account of the Kinetic Theory of Viscosity, Thermal Conduction, and Diffusion in Gases. The University Press, 1939.

[39] J. H. Lee. Basic governing equations for the flight regimes of aeroassisted orbital transfer vehicles. In *19th Thermophysics Conference*, 1984.

[40] J. D. Ramshaw and C. H. Chang. Ambipolar diffusion in multicomponent plasmas. *Plasma Chemistry and Plasma Processing*, 13(3):489–498, 1993.

[41] T. E. Magin and G. Degrez. Transport algorithms for partially ionized and unmagnetized plasmas. *Journal of Computational Physics*, 198(2):424–449, 2004.

[42] M. J. Wright, H. H. Hwang, and D. W. Schwenke. Recommended Collision Integrals for Transport Property Computations Part I: Air Species. *AIAA Journal*, 45(1):281–288, 2005.

[43] E. Levin and M. J. Wright. Collision Integrals for Ion-Neutral Interactions of Nitrogen and Oxygen. *Journal of Thermophysics and Heat Transfer*, 18(1):143–147, 2004.

[44] E. A. Mason. Transport Coefficients of Ionized Gases. *Physics of Fluids*, 10(8):1827, 1967.

[45] C. Park. *Non-Equilibrium Hypersonic Aerodynamics*. John Wiley & sons, New York, 1990.

[46] D. Bose and G. V. Candler. Thermal rate constants of the O2+N -> NO+O reaction based on the 2A' and 4A' potential-energy surfaces. *The Journal of Chemical Physics*, 107(16):6136–6145, 1997.

[47] C. Park. Review of chemical-kinetic problems of future NASA missions. I - Earth entries. *Journal of Thermophysics and Heat Transfer*, 7(3):385–398, 1993.

[48] T. E. Magin. *A Model for Inductive Plasma Wind Tunnels*. PhD thesis, ULB and VKI, 2004.

Appendices

A Nomenclature

Roman Symbols

A_r Pre-exponential reaction rate constant $[(\mathrm{m}^3/\mathrm{mol})^{\sum_s \nu'_{sr}-1}\ \mathrm{s}^{-1}\ \mathrm{K}^{-n_{T,r}}]$

a_0 $= \frac{\mathrm{Ec}_w}{1+\mathrm{Ec}/2} C$ [-]

a_1 $= C/\mathrm{Pr}$ [-]

a_2 $= \frac{\mathrm{Ec}}{1+\mathrm{Ec}/2}(C-a_1)$ [-]

$A^*_{s\ell}$ Ratio of collision integrals $(= \frac{\Omega^{(2,2)}_{s\ell}}{\Omega^{(1,1)}_{s\ell}})$ [-]

a_{1s} $= \frac{a_1}{1+\mathrm{Ec}/2}\frac{h_s}{h_e}$ [-]

$a_{2s\ell}$ $= \frac{C_{s\ell}}{1+\mathrm{Ec}/2}\frac{h_s}{h_e}$ [-]

$B^*_{s\ell}$ Ratio of collision integrals $(= \frac{5\Omega^{(1,2)}_{s\ell}-4\Omega^{(1,3)}_{s\ell}}{\Omega^{(1,1)}_{s\ell}})$ [-]

C Chapman-Rubesin parameter $(= \frac{\mu\rho}{\mu_e\rho_e})$ [-]

c_p Heat capacity at cst. pressure [J/kg-K]

$C^*_{s\ell}$ Ratio of collision integrals $(= \frac{\Omega^{(1,2)}_{s\ell}}{\Omega^{(1,1)}_{s\ell}})$ [-]

$C_{s\ell}$ $= \frac{C\rho\mathcal{D}_{s\ell}}{\mu}$ [-]

c_v Heat capacity at cst. volume [J/kg-K]

$\mathcal{D}_{s\ell}$ Multi-component diffusion coef. [m^2/s]

$\mathcal{D}_{\mathrm{eff},s}$ Effective diffusion coefficient [m^2/s]

$\mathscr{D}_{s\ell}$ Binary diffusion coefficient [m^2/s]

e Internal energy [J/kg]

Ec Streamwise Eckert number $(= u_e^2/h_e)$ [-]

Ec_w Spanwise Eckert number $(= w_0^2/h_e)$ [-]

f Streamfunction-related variable $(f_\eta = u/u_e)$ [-]

g $= H/H_e$ [-]

$G^\kappa_{s\ell}$ Heavy-particle translational thermal conductivity matrix subsystem [K m/W]

$G^\mu_{s\ell}$ Viscosity matrix subsystem [m s/kg]

g_{sm} Degeneracy of the m-th electronic energy level of species s [-]

$\hbar$ Planck's constant ($= 6.626070040 \cdot 10^{-34}$) [J s]

$\mathcal{H}$ Set of heavy species (not electrons) [-]

H Semi-total enthalpy ($= h + u^2/2$) [J/kg]

h Static enthalpy [J/kg]

$h^{\circ}_{f,s}$ Species formation enthalpy at 0K [J/kg]

$H^{298\,\mathrm{K}}_{f,s}$ Species formation enthalpy at 298K [J/mol]

j $= \rho_e/\rho$ [-]

J_s Mass diffusion flux [kg/m^2-s]

k $= w/w_0$ [-]

k_B Boltzmann's constant ($= 1.38064852 \cdot 10^{-23}$) [m^2 kg/K-s^2]

$k_{b,r}$ Backward reaction rate [(m^3/mol)$^{\sum_s \nu''_{sr}-1}$ s^{-1}]

K_{eq} Equilibrium constant [(m^3/mol)$^{\sum_s \nu'_{sr}-\nu''_{sr}}$]

$k_{f,r}$ Forward reaction rate [(m^3/mol)$^{\sum_s \nu'_{sr}-1}$ s^{-1}]

K_p Equilibrium pressure cst. [Pa$^{\sum_s \nu''_{sr}-\nu'_{sr}}$]

$\mathcal{L}_s$ Molecule's linearity factor (3 for non-linear and 2 for linear) [-]

L Wedge length [m]

M Mach number ($= u/\sqrt{\gamma R T}$) [-]

$\mathscr{M}$ Mixture molar mass ($= (\sum_{s\in\mathcal{S}} Y_s/\mathscr{M}_s)^{-1}$) [kg/mol]

$\mathscr{M}_s$ Species molar mass [kg/mol]

$\check{\mathscr{M}}_{s\ell}$ Species pair reduced molar mass [kg/mol]

n Number density [1/m^3]

N_A Avogadro's number ($= 6.022140857 \cdot 10^{23}$) [1/mol]

$n_{T,r}$ Temperature exponential reaction rate constant [-]

p Pressure [Pa]

Pr Prandtl number ($= \frac{\mu c_p}{\kappa}$) [-]

$\mathcal{Q}$ Partition function [-]

Q Arbitrary dependent flow variable

q Arbitrary independent flow variable

q_{e^-} Elementary charge ($= 1.6021766208981 \cdot 10^{-19}$) [C]

$\mathcal{R}$ Set of all reactions [-]

$\mathscr{R}$ Ideal gas constant ($= 8.31447$) [J/K-mol]

$\mathrm{Re}_{\mathscr{L}}$ Reynolds number based on $\mathscr{L}$ ($= \rho u \mathscr{L}/\mu$) [-]

$\mathcal{S}$ Set of all species [-]

$\mathcal{S}_{ion}$ Set of all ion species [-]

$\mathcal{S}_{mol}$ Set of all molecular species [-]

T Temperature [K]

t Time [s]

U Velocity normal to the shock [m/s]

u, v, w Velocity in x, y and z [m/s]

$\mathcal{X}_E$ Elemental fraction [-]

X_s Mole fraction [-]

x, y, z Streamwise, wall-normal and spanwise coordinates [m]

Y_s Mass fraction [-]

$\mathcal{Z}$ Unitary charge [-]

Greek Symbols

α Perturbation wavenumber in x [1/m]

β Perturbation wavenumber in z [1/m]

β_H Hartree's streamwise pressure gradient parameter ($= \frac{2\xi}{u_e}\frac{\mathrm{d}u_e}{\mathrm{d}\xi}$) [-]

γ Heat capacity ratio ($= \frac{c_p}{c_v}$) [-]

δ_{99} Boundary-layer height with the criterion of 99% of the total enthalpy [m]

$\delta_{s\ell}$ Dirac's delta symbol (1 for $s = \ell$, 0 otherwise) [-]

ε_0 Permittivity of vacuum ($= 8.854187817620 \cdot 10^{-12}$) [C^2/N-m^2]

ζ_s Ratio of mixture to species molar mass ($= \frac{\mathscr{M}}{\mathscr{M}_s}$) [-]

η Self-similar wall-normal variable ($d\eta = \frac{u_e}{\sqrt{2\xi}}\rho dy$) [-]

η_s^{μ} Mono-species shear viscosity coefficients [kg/m-s]

θ_{sm}^{Elec} Activation temperature of the m-th electronic energy level of species s [K]

θ_H Hartree's streamwise total enthalpy gradient parameter ($= \frac{2\xi}{H_e}\frac{dH_e}{d\xi}$) [-]

θ_r Reaction activation temperature [K]

θ_s^{Rot} Rotational activation temperature [K]

θ_s^{Vib} Vibrational activation temperature [K]

κ Thermal conductivity [W/K-m]

λ_D Debye shielding length [m]

μ Dynamic viscosity [kg/m-s]

ν'_{sr} Stoichiometric coefficient for reactants s in reaction r [-]

ν''_{sr} Stoichiometric coefficient for products s in reaction r [-]

ξ Marching streamwise variable ($d\xi = \rho_e \mu_e u_e dx$) [kg^2/m^2-s^2]

ρ Density [kg/m^3]

σ_s Molecule's steric factor (2 for symmetric, 1 for non-symmetric)[-]

χ Computational marching variable [-]

$\dot{\Omega}_s$ $= \frac{\dot{\omega}_s}{\rho \rho_e \mu_e u_e^2}$ [m^2 s^2/kg^2]

ω Perturbation frequency [1/s]

$\Omega_{s\ell}^{(i,j)}$ Collision integral (i,j) between species s and ℓ [m^2]

$\dot{\omega}_s$ Species mass source term [kg/m^3-s]

Sub- and superscripts

$\bar{q}$ Basic-state variable

q' Perturbation variable

$\tilde{q}$ Perturbation-amplitude variable

q_η, q_ξ Derivative with respect to η or ξ

q_e Boundary-layer edge value

q_{e^-} Referred to the electron species

q_∞ Freestream pre-shock quantity

q_r Reaction quantity

q^{Mod} Referred to the different energy modes

q_s, q_ℓ Species-specific quantity

$q_{s\ell}$ Species-pair-specific quantity

B Equilibrium relations

The obtention of the mixture composition in chemical equilibrium requires of the resolution of its corresponding equilibrium system. To have closure, it must necessarily have as many equations as species in the mixture.

For the air-5 mixture, three dissociation equilibrium relations are imposed together with the concentration condition, and with the elemental-fraction-ratio condition:

$$p X_{\mathrm{O}}^2 / X_{\mathrm{O}_2} = K_{p,\mathrm{O}_2}^{\mathrm{Diss}}(T)\,, \tag{7a}$$

$$p X_{\mathrm{N}}^2 / X_{\mathrm{N}_2} = K_{p,\mathrm{N}_2}^{\mathrm{Diss}}(T)\,, \tag{7b}$$

$$p X_{\mathrm{N}} X_{\mathrm{O}} / X_{\mathrm{NO}} = K_{p,\mathrm{NO}}^{\mathrm{Diss}}(T)\,, \tag{7c}$$

$$\sum_{s\in\mathcal{S}} X_s = 1\,, \tag{7d}$$

$$\frac{X_{\mathrm{O}} + 2X_{\mathrm{O}_2} + X_{\mathrm{NO}}}{X_{\mathrm{N}} + 2X_{\mathrm{N}_2} + X_{\mathrm{NO}}} = \mathcal{X}_{\mathrm{O}}/\mathcal{X}_{\mathrm{N}}\,. \tag{7e}$$

For the air-11 mixture, one must add the equilibrium relations for ionization reactions, and enforce the ambipolar condition:

$$p X_{\mathrm{O}}^2 / X_{\mathrm{O}_2} = K_{p,\mathrm{O}_2}^{\mathrm{Diss}}(T)\,, \tag{8a}$$

$$p X_{\mathrm{N}}^2 / X_{\mathrm{N}_2} = K_{p,\mathrm{N}_2}^{\mathrm{Diss}}(T)\,, \tag{8b}$$

$$p X_{\mathrm{N}} X_{\mathrm{O}} / X_{\mathrm{NO}} = K_{p,\mathrm{NO}}^{\mathrm{Diss}}(T)\,, \tag{8c}$$

$$p X_{O^+} X_{e^-} / X_O = K^{\text{Ioniz}}_{p,O}(T)\,, \tag{8d}$$

$$p X_{O_2^+} X_{e^-} / X_{O_2} = K^{\text{Ioniz}}_{p,O_2}(T)\,, \tag{8e}$$

$$p X_{N^+} X_{e^-} / X_N = K^{\text{Ioniz}}_{p,N}(T)\,, \tag{8f}$$

$$p X_{N_2^+} X_{e^-} / X_{N_2} = K^{\text{Ioniz}}_{p,N_2}(T)\,, \tag{8g}$$

$$p X_{NO^+} X_{e^-} / X_{NO} = K^{\text{Ioniz}}_{p,NO}(T)\,, \tag{8h}$$

$$\sum_{s\in\mathcal{S}} X_s = 1\,, \tag{8i}$$

$$\frac{X_O + 2X_{O_2} + X_{NO} + X_{O^+} + 2X_{O_2^+}}{X_{N^+} + 2X_{N_2^+} + X_{NO^+} + X_{N^+} + 2X_{N_2^+}} = \mathcal{X}_O/\mathcal{X}_N\,, \tag{8j}$$

$$\frac{X_{O^+} + X_{O_2^+} + X_{NO^+} + X_{N^+} + X_{N_2^+}}{X_{e^-}} = 1\,. \tag{8k}$$

where the Diss and Ioniz superscripts denote if the reaction is dissociative or ionizing.

Systems (7) and (8) are solved on the natural logarithms of the mole fractions to avoid numerical overflow and underflow. The equations are also linearized and solved using a Newton-Raphson iterative method.

Note that the equilibrium pressure constants $K_{p,r}$ are related to those defined in § D.5 (Eq. (37)) through:

$$K_{p,r} = K_{eq,r}\,(\mathscr{R}T)^{\sum_{s\in\mathcal{S}}(\nu''_{sr}-\nu'_{sr})}\,. \tag{9}$$

C Oblique shock relations

The shock jump relations are evaluated in agreement with the different flow assumptions. However, the equations to satisfy are in all cases the normal shock relations:

$$\rho_1 U_1 = \rho_2 U_2\,, \tag{10a}$$

$$p_1 + \rho_1 U_1^2 = p_2 + \rho_2 U_2^2\,, \tag{10b}$$

$$h_1 + U_1^2/2 = h_2 + U_2^2/2\,, \tag{10c}$$

which relate the preshock (1) and postshock (2) conditions, where the U velocity is oriented in the direction normal to the shock. The streamlines are assumed to be parallel to the wedge surface immediately after the shock.

The difference between the flow assumptions will be imposed in the evaluation of the enthalpy and the equation of state. For CPG, the shock is imposed vibrationally and chemically frozen, and therefore $c_{p,1} = c_{p,2}$ and $Y_{s,1} = Y_{s,2}$. For TPG, the shock is assumed in vibrational equilibrium, yet chemically frozen, and therefore $Y_{s,1} = Y_{s,2}$, yet the enthalpies are non-linear functions of T: $h_1 = h_1(T_1)$ and $h_2 = h_2(T_2)$, following the models detailed in appendix D. Finally, for LTE the shock is assumed in both vibrational and chemical equilibrium. The composition therefore depends on the pre-shock and post-shock pressure and temperature $Y_{s,1} = Y_{s,1}(p_1, T_1)$ and $Y_{s,2} = Y_{s,2}(p_2, T_2)$, through the equilibrium systems detailed in appendix B. The enthalpy therefore depends explicitly on T and implicitly on T and p through the equilibrium system $h_1 = h_1(T_1, Y_{s,1}(p_1, T_1))$ and $h_2 = h_2(T_2, Y_{s,2}(p_2, T_2))$.

The non-equilibrium shock notedly has a varying angle that varies from the TPG to the LTE angle. However, the present analysis of the inviscid flow field is restricted to the wall streamline. Therefore, the CNE shock angle can be taken identical to the TPG angle.

D Thermodynamic and transport models

D.1 Thermal models

The internal energy due to the different energy modes of the different gas species e_s^{Mod} can be obtained from the partition functions Q_s^{Mod}:

$$e_s^{Mod} = \frac{\mathscr{R}}{\mathscr{M}_s} T^2 \frac{\partial \ln Q_s^{Mod}}{\partial T}\,. \tag{11}$$

Subsequently, the heat capacity at constant volume of each energy mode is based on the internal energy as:

$$c_{vs}^{Mod} = \frac{\partial e_s^{Mod}}{\partial T}. \tag{12}$$

The partition functions of the translational, rotational, vibrational and electronic modes, neglecting the rotational energy of monoatomic species; assuming diatomic molecules to behave like rigid rotors and harmonic oscillators; and assuming a Boltzmann distribution of the electronic energy states are:

$$Q_s^{TransV} = \left(\frac{2\pi \mathscr{M}_s k_B T}{N_A \hbar^2}\right)^{\frac{3}{2}}, \tag{13a}$$

$$Q_s^{Rot} = \frac{1}{\sigma_s}\left(\frac{T}{\theta_s^{Rot}}\right)^{\mathcal{L}_s/2}, \quad \forall s \in \mathcal{S}_{mol}, \tag{13b}$$

$$Q_s^{Vib} = \frac{1}{1-\mathrm{e}^{-\theta_s^{Vib}/T}}, \quad \forall s \in \mathcal{S}_{mol}, \tag{13c}$$

$$Q_s^{Elec} = \sum_{m=0}^{\infty} g_{sm}\mathrm{e}^{-\theta_{sm}^{Elec}/T}, \quad \forall s \in \mathcal{H}, \tag{13d}$$

$$Q_{e^-}^{Int} = 2. \tag{13e}$$

The species properties appearing in these expressions (σ_s, $\mathcal{L}_s$, θ_s^{Rot}, θ_s^{Vib}, θ_{sm}^{Elec} and g_{sm}) are obtained from Ref. [36] and are tabled in tables 2-5.

Note that Eq. (13a) corresponds to the volumetric partition function of the translational energy, since it has been divided by the system's volume. Also note that the expression for the partition function of the electron species' internal energy $Q_{e^-}^{Int}$ (Eq. 13e) is formulated to account for the contribution of the spin of the free electron to the species entropy [35, 37].

From the internal energies of each energy mode for each species, considering a unique temperature for all the energy modes, one reaches that the species and mixture enthalpies are:

$$h_s = e_s^{Trans} + e_s^{Rot} + e_s^{Vib} + e_s^{Elec} + h_{f,s}^{\circ} + \mathscr{R}T, \tag{14}$$

$$h = \sum_{s\in\mathcal{S}} Y_s h_s. \tag{15}$$

The species formation enthalpy per mole at 298 K [36] $H_{f,s}^{298\,\mathrm{K}}$ is by convention 0 for N_2, O_2 and e^-, and it is obtained from a formation reaction for all other species (see table 2). The species formation enthalpies at 0 K are then obtained using Hess' law.

For the CPG cases, constant heat capacity and heat capacity ratios were used ($c_p = 1004.5$ J/kg-K and $\gamma = 1.4$).

D.2 Diffusion models

The binary diffusion coefficients $\mathscr{D}_{s\ell}$ are obtained from the first-order approximation to Chapman & Enskog's kinetic theory of dilute gases [38]:

$$\mathscr{D}_{s\ell} = \frac{1}{n}\sqrt{\frac{2\pi k_B T N_A}{\check{\mathscr{M}}_{s\ell}}}\frac{3}{16\pi\Omega_{s\ell}^{(1,1)}}, \forall s,\ell \in \mathcal{H}, \tag{16a}$$

$$\mathscr{D}_{se^-} = \frac{1}{n}\sqrt{\frac{2\pi k_B T N_A}{\mathscr{M}_{e^-}}}\frac{3}{16\pi\Omega_{se^-}^{(1,1)}}, \forall s \in \mathcal{H}, \tag{16b}$$

$$\mathscr{D}_{e^-e^-} = \frac{1}{n}\sqrt{\frac{\pi k_B T N_A}{\mathscr{M}_{e^-}}}\frac{3}{8\pi\Omega_{e^-e^-}^{(1,1)}}, \tag{16c}$$

where the reduced molar mass is:

$$\check{\mathscr{M}}_{s\ell} = \frac{\mathscr{M}_s \mathscr{M}_\ell}{\mathscr{M}_s + \mathscr{M}_\ell}. \tag{17}$$

The effective diffusion coefficients are then defined as:

$$\mathcal{D}_{\mathrm{eff},s} = \frac{1-X_s}{\sum_{\substack{\ell\in\mathcal{S}\\ \ell\neq s}} X_\ell/\mathscr{D}_{s\ell}}, \tag{18}$$

onto which one must impose Lee's correction [39] to account for the ambipolar condition:

$$\mathcal{D}_{\mathrm{eff},s}^{\text{ambip.}} \approx 2\,\mathcal{D}_{\mathrm{eff},s}^{\text{non-ambip.}}, \forall s \in \mathcal{S}_{ion}. \tag{19}$$

Finally, the multicomponent diffusion coefficients are obtained after imposing Ramshaw's correction [40]. This is done to ensure that the

sum of the diffusion fluxes is equal to zero, resulting in the Self-Consistent Effective Binary Ambipolar Diffusion (SCEBAD) coefficients:

$$\mathcal{D}_{s\ell} = \left(\delta_{s\ell} - Y_\ell\left(1 + Z_\ell\frac{\mathscr{M}_{e^-}}{\mathscr{M}_\ell}\right)\right)\frac{1}{X_\ell}\cdot \cdot \frac{1-Y_\ell}{1-X_\ell}\left(1-\delta_{e^-\ell}\right)\mathcal{D}_{\text{eff},\ell}\,,\ \forall s \in \mathcal{H}\,, \tag{20a}$$

$$\mathcal{D}_{e^-\ell} = \left(\left(1-Y_{e^-}\right)Z_\ell - Y_{e^-}\frac{\mathscr{M}_\ell}{\mathscr{M}_{e^-}}\right)\frac{1}{X_{e^-}}\cdot \cdot \frac{1-Y_\ell}{1-X_\ell}\left(1-\delta_{e^-\ell}\right)\mathcal{D}_{\text{eff},\ell}\,. \tag{20b}$$

D.3 Transport models

The expressions for the dynamic viscosity μ and heavy-particle translational thermal conductivity κ_H^{Trans} are obtained from the approximations of Chapman & Enskog's kinetic theory of dilute gases [38] using Laguerre-Sonine polynomials [41]. Both μ and κ_H^{Trans} are obtained by solving a matrix system:

$$\mu = -\begin{vmatrix} G^\mu_{s\ell} & X_s \\ X_\ell & 0 \end{vmatrix} / |G^\mu_{s\ell}|\,,\ \forall s,\ell \in \mathcal{H}\,, \tag{21}$$

$$\kappa_H^{Trans} = -\begin{vmatrix} G^\kappa_{s\ell} & X_s \\ X_\ell & 0 \end{vmatrix} / |G^\kappa_{s\ell}|\,,\ \forall s,\ell \in \mathcal{H}\,. \tag{22}$$

The elements of the matrix subsystems for the first approximation on μ and the second on κ_H^{Trans} are defined as [41]:

$$G^\mu_{s\ell} = \frac{X_s X_\ell}{n\mathscr{D}_{s\ell}}\frac{N_A}{\mathscr{M}_s+\mathscr{M}_\ell}\left(\frac{6}{5}A^*_{s\ell} - 2\right),\ \forall s \neq \ell\,, \tag{23a}$$

$$G^\mu_{ss} = \sum_{\substack{\ell\in\mathcal{H}\\ \ell\neq s}}\frac{X_s X_\ell}{n\mathscr{D}_{s\ell}}\frac{N_A}{\mathscr{M}_s+\mathscr{M}_\ell}\left(\frac{6\mathscr{M}_\ell}{5\mathscr{M}_s}A^*_{s\ell} + 2\right) + \frac{X_s^2}{\eta_s^\mu}\,, \tag{23b}$$

$$G^\kappa_{s\ell} = \frac{1}{25\,k_B}\frac{X_s X_\ell}{n\mathscr{D}_{s\ell}}\frac{\mathscr{M}_s\mathscr{M}_\ell}{\left(\mathscr{M}_s+\mathscr{M}_\ell\right)^2}\left(16A^*_{s\ell} + 12B^*_{s\ell} - 55\right),\ \forall s \neq \ell\,, \tag{24a}$$

$$G^\kappa_{ss} = \frac{1}{25\,k_B}\sum_{\substack{\ell\in\mathcal{H}\\ \ell\neq s}}\frac{X_s X_\ell}{n\mathscr{D}_{s\ell}}\frac{\mathscr{M}_s\mathscr{M}_\ell}{\left(\mathscr{M}_s+\mathscr{M}_\ell\right)^2}\left(16A^*_{s\ell} - 12\frac{\mathscr{M}_\ell}{\mathscr{M}_s}B^*_{s\ell} + 25\frac{\mathscr{M}_\ell}{\mathscr{M}_s} + 30\frac{\mathscr{M}_s}{\mathscr{M}_\ell}\right) + \frac{4}{15k_B}\frac{X_s^2\mathscr{M}_s}{N_A\eta_s^\mu}\,, \tag{24b}$$

where the mono-species shear viscosity coefficients are defined as:

$$\eta_s^\mu = \frac{5}{16}\frac{\sqrt{\pi k_B T\,\mathscr{M}_s/N_A}}{\pi\Omega^{(2,2)}_{ss}}\,. \tag{25}$$

The other components of the thermal conductivity are associated with the internal energy modes (κ^{Rot}, κ^{Vib} and κ^{Elec}) and with the electron thermal conductivity ($\kappa_{e^-}^{Trans}$). The former are obtained from Eucken's relation:

$$\kappa^{Rot} = \sum_{s\in\mathcal{S}_{mol}}\frac{\mathscr{M}_s}{N_A}\frac{X_s\,c^{Rot}_{v,s}}{\sum_{\ell\in\mathcal{H}}X_\ell/n\mathscr{D}_{s\ell}}\,, \tag{26a}$$

$$\kappa^{Vib} = \sum_{s\in\mathcal{S}_{mol}}\frac{\mathscr{M}_s}{N_A}\frac{X_s\,c^{Vib}_{v,s}}{\sum_{\ell\in\mathcal{H}}X_\ell/n\mathscr{D}_{s\ell}}\,, \tag{26b}$$

$$\kappa^{Elec} = \sum_{s\in\mathcal{H}}\frac{\mathscr{M}_s}{N_A}\frac{X_s\,c^{Elec}_{v,s}}{\sum_{\ell\in\mathcal{H}}X_\ell/n\mathscr{D}_{s\ell}}\,, \tag{26c}$$

where the product $\frac{\mathscr{M}_s}{N_A}c^{Mod}_{v,s}$ corresponds to the species specific heat per particle used by Magin [41].

The expression for the electron thermal conductivity, corresponding to the second approximation of the Laguerre-Sonine polynomials is given by [41]:

$$\kappa_{e^-}^{Trans} = \frac{X_{e^-}^2}{\Lambda^{11}_{e^-e^-}}\,, \tag{27}$$

where:

$$\Lambda^{11}_{e^-e^-} = \frac{64X_{e^-}}{75\,k_B}\sqrt{\frac{\mathscr{M}_s/N_A}{2\pi k_B T}}\left(\sum_{\ell\in\mathcal{H}}X_\ell\,\pi\left(\frac{25}{4}\Omega^{(1,1)}_{e^-\ell} - 15\Omega^{(1,2)}_{e^-\ell} + 12\Omega^{(1,3)}_{e^-\ell}\right) + X_{e^-}\sqrt{2}\,\Omega^{(2,2)}_{e^-e^-}\right). \tag{28}$$

Finally, the total mixture thermal conductivity is equal to:

$$\kappa = \kappa_H^{Trans} + \kappa_{e^-}^{Trans} + \kappa^{Rot} + \kappa^{Vib} + \kappa^{Elec} . \quad (29)$$

The Sutherland viscosity law used in § 3 is evaluated with the coefficients proposed by White [32].

D.4 Collision integrals

The evaluation of the expressions for viscosity μ, thermal conductivity κ and the diffusion coefficients $\mathcal{D}_{s\ell}$ (see § D.2 and D.3) requires collisional for the different species pairs. This collisional data is gathered from the work of a series of authors (Refs. [42, 43, 44]), and then polynomial-exponential functions are fitted to all of them:

$$\ln \Omega_{s\ell}^{(i,j)} = A^{\Omega_{s\ell}^{(i,j)}} + B^{\Omega_{s\ell}^{(i,j)}} \ln T + C^{\Omega_{s\ell}^{(i,j)}} (\ln T)^2 + \\ + D^{\Omega_{s\ell}^{(i,j)}} (\ln T)^3 + E^{\Omega_{s\ell}^{(i,j)}} (\ln T)^4 + F^{\Omega_{s\ell}^{(i,j)}} (\ln T)^5 . \quad (30)$$

This is done in order to have continuous thermodynamic derivatives of the different transport properties (e.g. $\partial\mu/\partial T$).

As detailed in § D.2 and D.3, the $\Omega_{s\ell}^{(1,1)}$, $\Omega_{s\ell}^{(2,2)}$, $\Omega_{s\ell}^{(1,2)}$ and $\Omega_{s\ell}^{(1,3)}$ collision integrals are required. $\Omega_{s\ell}^{(1,1)}$ and $\Omega_{s\ell}^{(2,2)}$ are fitted directly, whereas $\Omega_{s\ell}^{(1,3)}$ and $\Omega_{s\ell}^{(1,3)}$ are obtained from $B^*_{s\ell}$ and $C^*_{s\ell}$ (see appendix A). The curve-fit coefficients for $\Omega_{s\ell}^{(1,1)}$, $\Omega_{s\ell}^{(2,2)}$, $B^*_{s\ell}$ and $C^*_{s\ell}$ for the different pairs of species can be found in tables 6-19.

A special mention must be made regarding the charged-charged collisions, for which Eq. (30) is fitted to $[T^*; (T^*)^2\, \Omega_{s\ell}^{(i,j)}]$, $[T^*; B^*_{s\ell}]$ and $[T^*; C^*_{s\ell}]$ rather than $[T; \Omega_{s\ell}^{(i,j)}]$, $[T; B^*_{s\ell}]$ and $[T; C^*_{s\ell}]$. The reduced temperature T^* is defined as [44, 37]:

$$T^* = \frac{\lambda_D\, k_B\, T}{q_{e^-}^2/(4\pi\varepsilon_0)} , \quad (31)$$

where the Debye shielding length is defined as:

$$\lambda_D = \sqrt{\frac{\varepsilon_0\, k_B T}{2 q_{e^-}^2\, n_{e^-}}} . \quad (32)$$

The evaluation of the curve fits outside of the tabled range of temperatures could lead to extrapolation problems. In order to avoid this, additional fictitious points are added if necessary to the original set of data points before performing the fitting. For example, $e^- - NO$ collisions are only defined between 2000 and 20000 K [42]. In order to avoid extrapolation problems when evaluating them at 1000 K, additional points are added to Wright's dataset [42], such as $[1500\,\mathrm{K}; \Omega_{s\ell}^{(i,j)}|_{T=2000\,\mathrm{K}}]$ and $[1000\,\mathrm{K}; \Omega_{s\ell}^{(i,j)}|_{T=2000\,\mathrm{K}}]$. Depending on the dataset, the addition points are either "clipped off" (0^{th}-order extrapolation) or extrapolated linearly (1^{st}-order) from the last data points. This is done to preserve eventual clear trends in the data, and to avoid spurious oscillations in the fitting due to radical changes in these trends.

D.5 Chemical models

The species source terms for a set of chemical reactions of the form:

$$\sum_{s\in\mathcal{S}} \nu'_{sr}\, \mathcal{A}_s \leftrightarrow \sum_{s\in\mathcal{S}} \nu''_{sr}\, \mathcal{A}_s \quad , \quad \forall r \in \mathcal{R} , \quad (33)$$

are obtained from applying the law of mass action:

$$\dot{\omega}_s = \mathscr{M}_s \sum_{r\in\mathcal{R}} (\nu''_{sr} - \nu'_{sr}) \left(k_{f,r} \prod_{\ell\in\mathcal{S}} \left(\frac{\rho_\ell}{\mathscr{M}_\ell} \right)^{\nu'_{\ell r}} + \right. \\ \left. - k_{b,r} \prod_{\ell\in\mathcal{S}} \left(\frac{\rho_\ell}{\mathscr{M}_\ell} \right)^{\nu''_{\ell r}} \right) , \quad (34)$$

with the forward and backward reaction rates defined as:

$$k_{f,r} = A_r\, T^{n_{T,r}}\, \mathrm{e}^{-\theta_r/T} , \quad (35)$$

$$k_{b,r} = \frac{k_{f,r}}{K_{eq,r}} . \quad (36)$$

The equilibrium constant can be obtained from kinetic theory:

$$K_{eq,r} = \prod_{s\in\mathcal{S}} \left(\frac{\mathcal{Q}_s}{N_A} \right)^{\nu''_{sr} - \nu'_{sr}} \exp\left(-(\nu''_{sr} - \nu'_{sr}) \frac{h^\circ_{f,s}\, \mathscr{M}_s}{\mathscr{R}\, T} \right) , \quad (37)$$

where the partition function of a single species Q_s is equal to the product of those of the different energy modes:

$$Q_s = \prod_{Mod} Q_s^{Mod}. \tag{38}$$

Two sets of chemical reactions are considered in the present work for the two mixtures (air-5 and air-11). The reaction rates were obtained from Refs. [45, 46] and Ref. [47] respectively, and are detailed in tables 20 and 21.

Species	$\mathscr{M}_s$ [kg/mol]	$\mathcal{L}_s$ [-]	σ_s [-]	θ_s^{Rot} [K]	θ_s^{Vib} [K]	$H_{f,s}^{298\,\mathrm{K}}$ [J/mol]
N	0.014007					472440
O	0.015999					249229
N_2	0.028013	2	2	2.886	3408.464	0
O_2	0.031999	2	2	2.086	2276.979	0
NO	0.030006	2	1	2.464	2759.293	91089
N^+	0.014006					1881903
O^+	0.015999					1568841
N_2^+	0.028013	2	2	2.818	3253.157	1509509
O_2^+	0.031998	2	2	2.475	2887.139	1171413
NO^+	0.030006	2	1	2.892	3473.491	990653
e^-	5.5e-07					0

Table 2: Species properties taken from the mutation^{++} database [48, 37], gathered and adapted from Ref. [36].

	N		O		N^+		O^+	
m	$g_{N,m}$ [-]	$\theta_{N,m}^{Elec}$ [K]	$g_{O,m}$ [-]	$\theta_{O,m}^{Elec}$ [K]	$g_{N^+,m}$ [-]	$\theta_{N^+,m}^{Elec}$ [K]	$g_{O^+,m}$ [-]	$\theta_{O^+,m}^{Elec}$ [K]
0	4	0	9	0	1	0	4	0
1	10	27665	5	22861	3	70	6	38571
2	6	41497	1	48622	5	188	4	38602
3	12	119898	5	106136	5	22037	4	58223
4	6	124018	3	110487	1	47032	2	58225
5	12	126802	15	124633	5	67313		
6	2	134648	9	127535	7	132709		
7	20	136458	5	137374	5	132728		
8	12	137422	3	138442	3	132730		

Table 3: Atomic species' electronic levels taken from the mutation^{++} database [48, 37], gathered and adapted from Ref. [36].

	N		O	
m	$g_{\mathrm{N},m}$ [-]	$\theta^{Elec}_{\mathrm{N},m}$ [K]	$g_{\mathrm{O},m}$ [-]	$\theta^{Elec}_{\mathrm{O},m}$ [K]
9	4	139209	25	140299
10	10	139324	15	140415
11	6	140705	15	142737
12	10	143397	9	143548
13	12	149188	15	145637
14	6	149919	5	147030
15	6	150535	3	147493
16	28	150673	5	147842
17	26	150859	25	148075
18	20	151092	15	148190
19	10	151266	56	148306
20	2	153204	15	149234
21	20	153703	9	149582
22	12	153969	5	151207
23	10	154271	3	151440
24	4	154597	49	151788
25	6	154840	56	151869
26	12	158100	15	152368
27	6	158379	9	152485
28	90	158739	5	153413
29	126	158901	3	153529
30	24	159181	168	153761
31	2	159795	5	154689
32	38	160050	3	154805
33	4	160422	96	154956
34	10	160979	8	155640
35	6	161593	40	155710
36	18	162104	8	156186
37	60	162324	40	156244
38	126	162452	3	156581
39	32	163091	40	156615
40	18	164193		
41	90	164321		
42	180	164367		
43	20	164808		
44	108	165481		
45	18	166131		

Table 3: (cont.) Atomic species' electronic levels taken from the mutation^{++} database [48, 37], gathered and adapted from Ref. [36].

	N_2		O_2		NO	
m	$g_{N_2,m}$ [-]	$\theta^{Elec}_{N_2,m}$ [K]	$g_{O_2,m}$ [-]	$\theta^{Elec}_{O_2,m}$ [K]	$g_{NO,m}$ [-]	$\theta^{Elec}_{NO,m}$ [K]
0	1	0	3	0	4	0
1	3	72232	2	11392	8	54674
2	6	85779	1	18985		
3	6	86050	1	47560		
4	3	95351	6	49912		
5	1	98057	3	50923		
6	2	99683	3	71640		
7	2	103732				

Table 4: Molecular neutral species' electronic levels taken from the mutation^{++} database [48, 37], gathered and adapted from Ref. [36].

	N_2^+		O_2^+		NO^+	
m	$g_{N_2^+,m}$ [-]	$\theta^{Elec}_{N_2^+,m}$ [K]	$g_{O_2^+,m}$ [-]	$\theta^{Elec}_{O_2^+,m}$ [K]	$g_{NO^+,m}$ [-]	$\theta^{Elec}_{NO^+,m}$ [K]
0	2	0	4	0	1	0
1	4	13189	8	47354	3	75090
2	2	36633	4	58374	6	85212
3	4	36689	4	58414	6	89036
4	8	59853	6	62299	3	97470
5	8	66184			1	100055
6	4	75989			2	102804
7	4	76255			2	105713
8	4	82010				

Table 5: Molecular neutral species' electronic levels taken from the mutation^{++} database [48, 37], gathered and adapted from Ref. [36].

Pair	$A^{\Omega_{s\ell}^{(1,1)}}$	$B^{\Omega_{s\ell}^{(1,1)}}$	$C^{\Omega_{s\ell}^{(1,1)}}$	$D^{\Omega_{s\ell}^{(1,1)}}$
N – N	-3.9038e+01	-1.7537e+00	2.1127e-01	-9.6851e-03
N – O	-3.9926e+01	-1.3742e+00	1.6071e-01	-7.5128e-03
N – NO	-4.2197e+01	-4.2600e-01	3.7508e-02	-2.2969e-03
N – N_2	-3.8724e+01	-1.8610e+00	2.3616e-01	-1.1228e-02
N – O_2	-4.2744e+01	-2.6369e-01	1.7422e-02	-1.3345e-03
O – O	-3.9584e+01	-1.3768e+00	1.4468e-01	-6.3322e-03
O – NO	-4.2468e+01	-3.6840e-01	3.0304e-02	-1.8378e-03
O – N_2	-3.7564e+01	-2.3100e+00	2.7639e-01	-1.1946e-02
O – O_2	-4.0757e+01	-9.7101e-01	1.0277e-01	-4.8121e-03
NO – NO	-4.2358e+01	-2.8044e-01	1.8121e-02	-1.2700e-03
NO – N_2	-4.1948e+01	-4.7267e-01	4.8809e-02	-2.8408e-03
NO – O_2	-4.2201e+01	-3.3644e-01	2.2289e-02	-1.2450e-03
N_2 – N_2	-4.0494e+01	-1.0583e+00	1.2580e-01	-5.9892e-03
N_2 – O_2	-3.8991e+01	-1.5849e+00	1.7307e-01	-7.1877e-03
O_2 – O_2	-4.2101e+01	-3.7136e-01	2.3946e-02	-1.1232e-03

Table 6: Polynomial-logarithmic curve-fit coefficients for $\Omega_{s\ell}^{(1,1)}(T)$ of neutral-neutral collisions. Original data from Ref. [42].

Pair	$A^{\Omega_{s\ell}^{(1,1)}}$	$B^{\Omega_{s\ell}^{(1,1)}}$	$C^{\Omega_{s\ell}^{(1,1)}}$	$D^{\Omega_{s\ell}^{(1,1)}}$	$E^{\Omega_{s\ell}^{(1,1)}}$	$F^{\Omega_{s\ell}^{(1,1)}}$
Rep.	-1.3893e+00	7.9831e-01	-9.8424e-02	6.9179e-03	-2.4297e-04	3.3109e-06
Att.	-8.1744e-01	5.9718e-01	-7.7407e-02	6.3478e-03	-2.5986e-04	4.0068e-06

Table 7: Polynomial-logarithmic curve-fit coefficients for $(T^*)^2\,\Omega_{s\ell}^{(1,1)}(T^*)$ of charged-charged collisions (attractive and repulsive). Original data from Ref. [44]

.

Pair	$A^{\Omega_{s\ell}^{(1,1)}}$	$B^{\Omega_{s\ell}^{(1,1)}}$	$C^{\Omega_{s\ell}^{(1,1)}}$	$D^{\Omega_{s\ell}^{(1,1)}}$	$E^{\Omega_{s\ell}^{(1,1)}}$	$F^{\Omega_{s\ell}^{(1,1)}}$
N – e^-	3.2281e+02	-2.4904e+02	6.7663e+01	-9.0938e+00	6.0146e-01	-1.5649e-02
O – e^-	-4.7782e+01	7.3464e-02	3.3446e-02	-2.1165e-03		
NO – e^-	-3.0735e+02	1.8481e+02	-5.1335e+01	7.0356e+00	-4.7545e-01	1.2666e-02
N_2 – e^-	-4.2545e+01	-2.4080e+00	4.5715e-01	-2.3996e-02		
O_2 – e^-	-4.6532e+01	-7.1295e-01	2.0169e-01	-1.1934e-02		

Table 8: Polynomial-logarithmic curve-fit coefficients for $\Omega_{s\ell}^{(1,1)}(T)$ of electron-neutral collisions. Original data from Ref. [42].

Pair	$A^{\Omega_{s\ell}^{(1,1)}}$	$B^{\Omega_{s\ell}^{(1,1)}}$	$C^{\Omega_{s\ell}^{(1,1)}}$	$D^{\Omega_{s\ell}^{(1,1)}}$
$N - N^+$	-3.7581e+01	-1.6448e+00	1.8683e-01	-7.5578e-03
$N - O^+$	-2.4775e+01	-6.7148e+00	8.1943e-01	-3.4978e-02
$N - NO^+$	-3.1961e+01	-3.2668e+00	2.8783e-01	-8.5854e-03
$N - N_2^+$	-3.0760e+01	-3.9510e+00	4.0191e-01	-1.4068e-02
$N - O_2^+$	-3.9579e+01	-1.2054e-01	-1.3596e-01	9.6694e-03
$O - N^+$	-2.7402e+01	-5.7465e+00	7.0483e-01	-3.0935e-02
$O - O^+$	-3.8131e+01	-1.5362e+00	1.7325e-01	-6.9344e-03
$O - NO^+$	-2.9685e+01	-4.2924e+00	4.2837e-01	-1.4818e-02
$O - N_2^+$	-3.0158e+01	-4.3173e+00	4.5831e-01	-1.6786e-02
$O - O_2^+$	-3.6448e+01	-1.4838e+00	4.6679e-02	1.7505e-03
$NO - N^+$	-3.9487e+01	-1.2764e-03	-1.5636e-01	1.0702e-02
$NO - O^+$	-4.1206e+01	7.2851e-01	-2.5547e-01	1.4921e-02
$NO - NO^+$	-3.6146e+01	-2.0148e+00	2.1474e-01	-8.1158e-03
$NO - N_2^+$	-3.3071e+01	-2.7592e+00	2.2605e-01	-6.0142e-03
$NO - O_2^+$	-4.3769e+01	1.7367e+00	-3.8451e-01	2.0239e-02
$N_2 - N^+$	-4.0019e+01	1.7359e-01	-1.7473e-01	1.1292e-02
$N_2 - O^+$	-4.2235e+01	1.1468e+00	-3.0975e-01	1.7178e-02
$N_2 - NO^+$	-3.7508e+01	-7.4474e-01	-6.2442e-02	6.8725e-03
$N_2 - N_2^+$	-4.0546e+01	-2.4688e-01	-1.6702e-02	1.8476e-03
$N_2 - O_2^+$	-4.2731e+01	1.4019e+00	-3.4757e-01	1.8825e-02
$O_2 - N^+$	-3.8651e+01	-3.3322e-01	-1.1476e-01	8.9703e-03
$O_2 - O^+$	-4.0448e+01	5.5155e-01	-2.4522e-01	1.4867e-02
$O_2 - NO^+$	-3.5265e+01	-1.6861e+00	6.2901e-02	1.4568e-03
$O_2 - N_2^+$	-3.5708e+01	-1.6861e+00	8.3471e-02	1.3455e-04
$O_2 - O_2^+$	-3.6074e+01	-2.0758e+00	2.2750e-01	-8.9521e-03

Table 9: Polynomial-logarithmic curve-fit coefficients for $\Omega_{s\ell}^{(1,1)}(T)$ of ion-neutral collisions. Original data from Ref. [43].

Pair	$A^{\Omega_{s\ell}^{(2,2)}}$	$B^{\Omega_{s\ell}^{(2,2)}}$	$C^{\Omega_{s\ell}^{(2,2)}}$	$D^{\Omega_{s\ell}^{(2,2)}}$
N – N	-3.9544e+01	-1.4745e+00	1.7016e-01	-7.6824e-03
N – O	-4.1206e+01	-8.5985e-01	9.7252e-02	-4.8372e-03
N – NO	-4.2196e+01	-3.7564e-01	3.1628e-02	-1.9878e-03
N – N_2	-3.9525e+01	-1.4870e+00	1.8326e-01	-8.5684e-03
N – O_2	-4.2785e+01	-2.0080e-01	1.0094e-02	-9.8152e-04
O – O	-4.0393e+01	-1.0303e+00	1.0124e-01	-4.4392e-03
O – NO	-4.2376e+01	-3.5586e-01	2.9098e-02	-1.7302e-03
O – N_2	-3.8745e+01	-1.7766e+00	2.0368e-01	-8.6395e-03
O – O_2	-4.1346e+01	-7.2951e-01	7.5403e-02	-3.6865e-03
NO – NO	-3.8671e+01	-1.7290e+00	2.0907e-01	-9.3898e-03
NO – N_2	-3.9328e+01	-1.4954e+00	1.8442e-01	-8.6334e-03
NO – O_2	-3.8881e+01	-1.6391e+00	1.9446e-01	-8.5899e-03
N_2 – N_2	-3.9501e+01	-1.3977e+00	1.6674e-01	-7.4713e-03
N_2 – O_2	-3.8863e+01	-1.6253e+00	1.8175e-01	-7.6114e-03
O_2 – O_2	-3.9060e+01	-1.5600e+00	1.8101e-01	-7.8269e-03

Table 10: Polynomial-logarithmic curve-fit coefficients for $\Omega_{s\ell}^{(2,2)}(T)$ of neutral-neutral collisions. Original data from Ref. [42].

Pair	$A^{\Omega_{s\ell}^{(2,2)}}$	$B^{\Omega_{s\ell}^{(2,2)}}$	$C^{\Omega_{s\ell}^{(2,2)}}$	$D^{\Omega_{s\ell}^{(2,2)}}$	$E^{\Omega_{s\ell}^{(2,2)}}$	$F^{\Omega_{s\ell}^{(2,2)}}$
Rep.	-1.1054e+00	7.6915e-01	-1.0322e-01	7.8798e-03	-2.9573e-04	4.2347e-06
Att.	-8.4402e-01	7.1378e-01	-1.0884e-01	9.5968e-03	-4.0386e-04	6.2833e-06

Table 11: Polynomial-logarithmic curve-fit coefficients for $(T^*)^2\,\Omega_{s\ell}^{(2,2)}(T^*)$ of charged-charged collisions (attractive and repulsive). Original data from Ref. [44]

.

Pair	$A^{\Omega_{s\ell}^{(2,2)}}$	$B^{\Omega_{s\ell}^{(2,2)}}$	$C^{\Omega_{s\ell}^{(2,2)}}$	$D^{\Omega_{s\ell}^{(2,2)}}$	$E^{\Omega_{s\ell}^{(2,2)}}$	$F^{\Omega_{s\ell}^{(2,2)}}$
N – e^-	2.8065e+02	-2.2550e+02	6.2339e+01	-8.5260e+00	5.7519e-01	-1.5306e-02
O – e^-	-4.5517e+01	-1.0845e+00	2.1308e-01	-1.0341e-02		
NO – e^-	-2.5538e+01	-9.7678e+00	2.0119e+00	-1.8704e-01	6.4026e-03	
N_2 – e^-	-3.9665e+01	-3.8037e+00	6.6849e-01	-3.4152e-02		
O_2 – e^-	-4.6161e+01	-8.7392e-01	2.1951e-01	-1.2297e-02		

Table 12: Polynomial-logarithmic curve-fit coefficients for $\Omega_{s\ell}^{(2,2)}(T)$ of electron-neutral collisions. Original data from Ref. [42].

Pair	$A^{\Omega^{(2,2)}_{s\ell}}$	$B^{\Omega^{(2,2)}_{s\ell}}$	$C^{\Omega^{(2,2)}_{s\ell}}$	$D^{\Omega^{(2,2)}_{s\ell}}$
$N-N^+$	-3.5655e+01	-2.6192e+00	3.1296e-01	-1.4154e-02
$N-O^+$	-2.7101e+01	-5.6130e+00	6.4943e-01	-2.6411e-02
$N-NO^+$	-3.5063e+01	-2.0536e+00	1.3379e-01	-2.0391e-03
$N-N_2^+$	-3.2163e+01	-3.3751e+00	3.2708e-01	-1.0814e-02
$N-O_2^+$	-4.3694e+01	1.4961e+00	-3.4166e-01	1.8378e-02
$O-N^+$	-2.6016e+01	-6.2810e+00	7.6979e-01	-3.3287e-02
$O-O^+$	-2.8235e+01	-5.4331e+00	6.5900e-01	-2.8310e-02
$O-NO^+$	-3.0801e+01	-3.8751e+00	3.7871e-01	-1.2748e-02
$O-N_2^+$	-3.0335e+01	-4.2616e+00	4.5474e-01	-1.6691e-02
$O-O_2^+$	-3.8981e+01	-4.4644e-01	-8.8995e-02	7.6733e-03
$NO-N^+$	-4.3692e+01	1.6115e+00	-3.5785e-01	1.9110e-02
$NO-O^+$	-4.7030e+01	2.9527e+00	-5.3309e-01	2.6467e-02
$NO-NO^+$	-4.0053e+01	1.5830e-01	-1.6787e-01	1.1116e-02
$NO-N_2^+$	-3.6067e+01	-1.5874e+00	7.7506e-02	2.6752e-04
$NO-O_2^+$	-4.8999e+01	3.7342e+00	-6.3344e-01	3.0586e-02
N_2-N^+	-4.3063e+01	1.3742e+00	-3.2743e-01	1.7782e-02
N_2-O^+	-4.7022e+01	2.9653e+00	-5.3518e-01	2.6519e-02
N_2-NO^+	-4.0079e+01	2.1013e-01	-1.7820e-01	1.1642e-02
$N_2-N_2^+$	-3.6490e+01	-1.3785e+00	4.7018e-02	1.6350e-03
$N_2-O_2^+$	-4.8927e+01	3.7466e+00	-6.3810e-01	3.0838e-02
O_2-N^+	-4.2788e+01	1.2480e+00	-3.1164e-01	1.7169e-02
O_2-O^+	-4.4465e+01	2.0147e+00	-4.2055e-01	2.1971e-02
O_2-NO^+	-3.8771e+01	-3.6570e-01	-9.9550e-02	8.1846e-03
$O_2-N_2^+$	-3.5678e+01	-1.7099e+00	8.9315e-02	-1.1867e-04
$O_2-O_2^+$	-4.7599e+01	3.2565e+00	-5.8087e-01	2.8664e-02

Table 13: Polynomial-logarithmic curve-fit coefficients for $\Omega^{(2,2)}_{s\ell}(T)$ of ion-neutral collisions. Original data from Ref. [43].

Pair	$A^{B^*_{s\ell}}$
Neutral-neutral	1.3976e-01
Ion-neutral	1.8232e-01

Table 14: Polynomial-logarithmic curve-fit coefficients for $B^*_{s\ell}(T)$ of neutral-neutral and ion-neutral collisions. Original data from Refs. [42, 43].

Pair	$A^{B^*_{s\ell}}$	$B^{B^*_{s\ell}}$	$C^{B^*_{s\ell}}$	$D^{B^*_{s\ell}}$	$E^{B^*_{s\ell}}$	$F^{B^*_{s\ell}}$
Rep.	3.2065e-01	-2.2712e-02	-7.5168e-03	1.2584e-03	-6.5908e-05	1.1296e-06
Att.	2.8246e-01	-4.4970e-02	2.7922e-03	-5.6530e-05		

Table 15: Polynomial-logarithmic curve-fit coefficients for $B^*_{s\ell}(T^*)$ of charged-charged collisions (attractive and repulsive). Original data from Ref. [44]

.

Pair	$A^{B^*_{s\ell}}$	$B^{B^*_{s\ell}}$	$C^{B^*_{s\ell}}$	$D^{B^*_{s\ell}}$	$E^{B^*_{s\ell}}$	$F^{B^*_{s\ell}}$
$N - e^-$	1.8060e+02	-1.2272e+02	3.3368e+01	-4.4778e+00	2.9474e-01	-7.5949e-03
$O - e^-$	1.2037e+00	-7.9615e-01	1.2980e-01	-6.3897e-03		
$NO - e^-$	-3.3553e+02	2.3468e+02	-6.5098e+01	8.9211e+00	-6.0286e-01	1.6062e-02
$N_2 - e^-$	1.5552e+01	-1.2762e+01	4.3443e+00	-7.4972e-01	6.3606e-02	-2.0864e-03
$O_2 - e^-$	2.7998e-01	-1.1538e+00	2.4472e-01	-1.3242e-02		

Table 16: Polynomial-logarithmic curve-fit coefficients for $B^*_{s\ell}(T)$ of electron-neutral collisions. Original data from Ref. [42].

Pair	$A^{C^*_{s\ell}}$
Neutral-neutral	-8.3382e-02
Ion-neutral	-1.6252e-01

Table 17: Polynomial-logarithmic curve-fit coefficients for $C^*_{s\ell}(T)$ of neutral-neutral and ion-neutral collisions. Original data from Refs. [42, 43].

Pair	$A^{C^*_{s\ell}}$	$B^{C^*_{s\ell}}$	$C^{C^*_{s\ell}}$	$D^{C^*_{s\ell}}$	$E^{C^*_{s\ell}}$	$F^{C^*_{s\ell}}$
Rep.	-5.1112e-01	-1.0289e-01	3.0725e-03	5.9415e-04	-4.6560e-05	9.1973e-07
Att.	-6.4209e-01	-1.0884e-01	1.6057e-02	-1.3312e-03	5.4170e-05	-8.2828e-07

Table 18: Polynomial-logarithmic curve-fit coefficients for $C^*_{s\ell}(T^*)$ of charged-charged collisions (attractive and repulsive). Original data from Ref. [44]

.

Pair	$A^{C^*_{s\ell}}$	$B^{C^*_{s\ell}}$	$C^{C^*_{s\ell}}$	$D^{C^*_{s\ell}}$	$E^{C^*_{s\ell}}$	$F^{C^*_{s\ell}}$
$N - e^-$	1.3920e+02	-1.0077e+02	2.8664e+01	-4.0256e+00	2.7923e-01	-7.6490e-03
$O - e^-$	-6.3155e-01	3.3775e-01	-4.9419e-02	2.2542e-03		
$NO - e^-$	-2.9473e+00	2.3549e+00	-4.1738e-01	2.1115e-02		
$N_2 - e^-$	4.4244e-01	-1.4161e-01	2.7793e-02	-1.9415e-03		
$O_2 - e^-$	-5.1691e-01	4.5219e-01	-7.6554e-02	3.6272e-03		

Table 19: Polynomial-logarithmic curve-fit coefficients for $C^*_{s\ell}(T)$ of electron-neutral collisions. Original data from Ref. [42].

Reaction	M	A_r [(m^3/mol)$^{\sum_s \nu'_{sr}-1}$/s-K$^{n_{T,r}}$]	$n_{T,r}$ [-]	θ_r [K]
$N_2 + M \leftrightarrow 2N + M$	N	3.00e+16	-1.6	113200
	O	3.00e+16		
	NO	7.00e+15		
	N_2	7.00e+15		
	O_2	7.00e+15		
$O_2 + M \leftrightarrow 2O + M$	N	1.00e+16	-1.5	59360
	O	1.00e+16		
	NO	2.00e+15		
	N_2	2.00e+15		
	O_2	2.00e+15		
$NO + M \leftrightarrow N + O + M$	N	1.00e+11	0	75500
	O	1.00e+11		
	NO	1.00e+11		
	N_2	5.00e+09		
	O_2	5.00e+09		
$O + N_2 \leftrightarrow N + NO$		5.69e+06	0.42	42938
$O_2 + N \leftrightarrow NO + O$		2.49e+03	1.18	4005.5

Table 20: Air-5 reaction rate constants. Dissociation reactions taken from Park [45] and exchange from Bose & Candler [46].

Reaction	M	A_r [(m^3/mol)$^{\sum_s \nu'_{sr}-1}$/s-K$^{n_{T,r}}$]	$n_{T,r}$ [-]	θ_r [K]
$N_2 + M \leftrightarrow 2N + M$	N	3.00e+16	-1.6	113200
	O	3.00e+16		
	N_2	7.00e+15		
	O_2	7.00e+15		
	NO	7.00e+15		
	N^+	3.00e+16		
	O^+	3.00e+16		
	N_2^+	7.00e+15		
	O_2^+	7.00e+15		
	NO^+	7.00e+15		
	e^-	3.00e+18		
$O_2 + M \leftrightarrow 2O + M$	N	1.00e+16	-1.5	59500
	O	1.00e+16		
	N_2	2.00e+15		
	O_2	2.00e+15		
	NO	2.00e+15		
	N^+	1.00e+16		
	O^+	1.00e+16		
	N_2^+	2.00e+15		
	O_2^+	2.00e+15		
	NO^+	2.00e+15		
	e^-	0.00e+00		
$NO + M \leftrightarrow N + O + M$	N	1.10e+11	0	75500
	O	1.10e+11		
	N_2	5.00e+09		
	O_2	5.00e+09		
	NO	1.10e+11		
	N^+	1.10e+11		
	O^+	1.10e+11		
	N_2^+	5.00e+09		
	O_2^+	5.00e+09		
	NO^+	5.00e+09		
	e^-	0.00e+00		

Table 21: Air-11 reaction rate constants taken from Park [47].

Reaction	A_r [(m^3/mol)$^{\sum_s \nu'_{sr}-1}$/s-K$^{n_{T,r}}$]	$n_{T,r}$ [-]	θ_r [K]
$NO + O \leftrightarrow N + O_2$	8.40e+06	0	19450
$N_2 + O \leftrightarrow NO + N$	6.40e+11	-1	38400
$N + O \leftrightarrow NO^+ + e^-$	8.80e+02	1	31900
$O + O \leftrightarrow O_2^+ + e^-$	7.10e-04	2.7	80600
$N + N \leftrightarrow N_2^+ + e^-$	4.40e+01	1.5	67500
$NO^+ + O \leftrightarrow N^+ + O_2$	1.00e+06	0.5	77200
$N^+ + N_2 \leftrightarrow N_2^+ + N$	1.00e+06	0.5	12200
$O_2^+ + N \leftrightarrow N^+ + O_2$	8.70e+07	0.14	28600
$O^+ + NO \leftrightarrow N^+ + O_2$	1.40e-01	1.9	26600
$O_2^+ + N_2 \leftrightarrow N_2^+ + O_2$	9.90e+06	0	40700
$O_2^+ + O \leftrightarrow O^+ + O_2$	4.00e+06	-0.09	18000
$NO^+ + N \leftrightarrow O^+ + N_2$	3.40e+07	-1.08	12800
$NO^+ + O_2 \leftrightarrow O_2^+ + NO$	2.40e+07	0.41	32600
$NO^+ + O \leftrightarrow O_2^+ + N$	7.20e+06	0.29	48700
$O^+ + N_2 \leftrightarrow N_2^+ + O$	9.10e+05	0.36	22800
$NO^+ + N \leftrightarrow N_2^+ + O$	7.20e+07	0	35500
$O + e^- \leftrightarrow O^+ + 2e^-$	3.90e+27	-3.78	158500
$N + e^- \leftrightarrow N^+ + 2e^-$	2.50e+28	-3.82	168600

Table 21: (cont.) Air-11 reaction rate constants taken from Park [47].